Evaluation and Improvement of Methods for Estimating Sea Surface Wave Parameters From X-band Marine Radar Data

by

© **Zhiding Yang, B.Eng.**

A thesis submitted to the School of
Graduate Studies in partial
fulfillment of the requirements for
the degree of Master of Engineering.

Department of Electrical and Computer Engineering
Faculty of Engineering and Applied Science
Memorial University

May 2022

St. John's, Newfoundland and Labrador, Canada

Abstract

In this thesis, several algorithms have been proposed for estimating ocean wave parameters from X-band marine radar data, i.e., wave direction, wave period, and significant wave height. In the first part of this study, the accuracy of wave direction and period estimation from X-band marine radar images under different rain rates is analyzed, and a sub-image selection scheme is proposed to mitigate the rain effect. Firstly, each radar image is divided into multiple sub-images, and the sub-images with relatively clear wave signatures are identified based on a random-forest based classification model. Then, wave direction is estimated by performing a Radon transform (RT) on each valid sub-image. As for wave period estimation, a random-forest based regression method is proposed. Texture features are first extracted from each pixel of the selected sub-image using the gray-level co-occurrence matrix (GLCM) and combined as a feature vector. Those feature vectors extracted from both rain-free and rain-contaminated training samples are then used to train a random-forest based wave period regression model. Shore-based X-band marine radar images, simultaneous rain rate data, as well as buoy-measured wave data collected on the West Coast of the United States are used to analyze the rain effect on wave parameter estimation accuracy and to validate the proposed method. Experimental results show that the proposed sub-image selection scheme improves the estimation accuracy of both wave direction and wave period under different rain rates, with reductions of root-mean-square errors (RMSEs) by 6.9°, 6.0°, 4.9°, and 1.0° for wave direction under rainless, light rain, moderate rain, and heavy rain conditions, respectively. As for wave period estimation, the RMSEs decrease by 0.13 s, 0.20 s, 0.30 s, and 0.20 s under those four rainfall intensity levels, respectively.

The second part of research focuses on the estimation of significant wave height (H_s). A temporal convolutional network (TCN)-based model is proposed to retrieve H_s from X-band marine radar image sequences. Three types of features are first extracted from radar image sequences based on signal to noise ratio (SNR), ensemble empirical mode decomposition (EEMD), and GLCM methods, respectively. Then, feature vectors are input into the

proposed TCN-based regression model to produce H_s estimation. Radar data are collected from a moving vessel at the East Coast of Canada, as well as simultaneously collected wave data from several wave buoys deployed nearby are used for model training and testing. After averaging, experimental results show that the TCN-based model further improves the H_s estimation accuracy, with reductions of RMSEs by 0.33 m and 0.10 m, respectively, compared to the SNR-based and the EEMD-based linear fitting methods. It has also been found that with the same feature extraction scheme, TCN outperforms other machine-learning based algorithms including support vector regression (SVR) and the convolutional gated recurrent unit (CGRU) network.

Acknowledgements

The author would like to thank the Faculty of Engineering and Applied Science for providing the opportunity to study and research. Particularly, I would like to express my sincere gratitude to my supervisor, Dr. Weimin Huang. During the two-year study, he continuously provided me guidance and help. His patience and encouragement made me more confident for research and inspired me all the time. Besides, I am greatly appreciated that Dr. Xinwei Chen provided many useful suggestions and insights during the research and paper writing period.

The work was supported by the Natural Sciences and Engineering Research Council of Canada Discovery Grants under Grant NSERC RGPIN-2017-04508 and Grant RGPAS-2017-507962 to Dr. Weimin Huang. In addition, I would like to thank Dr. M. C. Haller of Oregon State University for providing the radar, anemometer, rain gauge, and buoy data, and thank Dr. E. Thornhill from DRDC for the provision of the radar and buoy data as well.

Moreover, I would also like to thank all the members of the radar remote sensing group and all my friends who have supported me on my way and pushed me to perform at my best. Finally, I would express my deep gratitude to my parents, Mr. Jingjian Yang and Mrs. Man Zhou. None of this work could be completed without their patience, support and understanding.

Table of contents

Title page **i**

Abstract **ii**

Acknowledgements **iv**

Table of contents **v**

List of tables **viii**

List of figures **ix**

List of symbols **xii**

List of abbreviations **xv**

1 Introduction **1**

1.1 Research Rationale 1

1.2 Literature Review 3

1.3 Motivation and Objectives 8

1.4 The Scope of the Thesis 9

2 Evaluation and Mitigation of Rain Effect on Wave Direction and Period Estimation from X-band Marine Radar Images 11

2.1 Data overview . . . 12

2.2 Methodology . . . 13

2.2.1 Sub-image Selection . . . 14

2.2.2 Wave Direction Estimation . . . 21

2.2.3 Wave Period Estimation . . . 24

2.3 Experimental Results . . . 26

2.3.1 The Influence of Rain on Extracted Features . . . 26

2.3.2 Wave Direction Result Analysis . . . 35

2.3.3 Wave Period Result Analysis . . . 38

2.4 Chapter Summary . . . 41

3 Wave Height Estimation from X-band Nautical Radar Images Using Temporal Convolutional Network 43

3.1 Data Overview . . . 43

3.2 Methodology . . . 44

3.2.1 Feature Extraction . . . 44

3.2.2 TCN-based Wave Height Estimation Model . . . 52

3.3 Experimental Results . . . 57

3.3.1 Model Training . . . 57

3.3.2 Input Features Validity Analysis . . . 57

3.3.3 Comparisons with Different Methods . . . 58

3.4 Chapter Summary 61

4 Conclusion **63**

4.1 Summary 63

4.2 Future Work 65

Bibliography **66**

List of tables

2.1 Radar information 13

2.2 RMSEs and CCs of wave direction estimation under different rainfall intensities 38

2.3 RMSEs and CCs of wave period estimation under different rainfall intensities 41

3.1 Radar information 45

3.2 RMSE comparison of estimated H_s for different input features 57

3.3 Comparisons of results using different methods for H_s estimation 61

List of figures

2.1 Locations of the radar, buoy, and weather station site as well as the bathymetry of the region from GPS Nautical Charts [1]. 12

2.2 Framework of wave direction and period estimation. 14

2.3 Radar images obtained under different simultaneous rainfall intensities: (a) rainless, (b) 1.5 mm/h rain rate, (c) 3.0 mm/h rain rate, (d) 9.1 mm/h rain rate. 15

2.4 Selection of 15 sub-images (outlined in red) in the radar image. 16

2.5 The pixel pairs in four directions having the same Chebyshev distance. 18

2.6 Valid sub-images (outlined in red) identified from radar image in Fig. 2.4. . . 21

2.7 (a) The valid sub-image highlighted in yellow dash lines in Fig. 2.6. (b) The detected edge image of (a). 22

2.8 (a) The RT results of all projection lines in Fig. 2.7(b). (b) The standard deviation of RT results as a function of projection direction. 23

2.9 The region extraction for wave period estimation. (a) The selected valid sub-image centering at A. (b) The extracted region centering at A for wave period estimation outlined in blue. 24

2.10 Box plots of the mean contrast distributions for different (a) wind speeds, (b) ranges, and (c) directions. 27

2.11 Box plots of the mean homogeneity distributions for different (a) wind speeds, (b) ranges, and (c) directions. 28

2.12 Box plots of the mean correlation distributions for different (a) wind speeds, (b) ranges, and (c) directions. 29

2.13 Box plots of the mean energy distributions for different (a) wind speeds, (b) ranges, and (c) directions. 30

2.14 Box plots of the standard deviation distribution of contrast for different (a) wind speeds, (b) ranges, and (c) directions. 31

2.15 Box plots of the standard deviation distribution of homogeneity for different (a) wind speeds, (b) ranges, and (c) directions. 32

2.16 Box plots of the standard deviation distribution of correlation for different (a) wind speeds, (b) ranges, and (c) directions. 33

2.17 Box plots of the standard deviation distribution of energy for different (a) wind speeds, (b) ranges, and (c) directions. 34

2.18 (a) Simultaneous wind speed and wave height during radar data collection periods. (b) Wave direction estimated with and without the sub-image selection scheme under rainless conditions. (c) Scatter plot of the radar-derived and buoy-measured wave direction under rainless conditions. 36

2.19 (a) Simultaneous wind speed and wave height during radar data collection periods. (b) Simultaneous rain rates during radar data collection periods. (c) Wave direction estimated with and without the sub-image selection scheme under rainfall conditions. (d) Scatter plot of the radar-derived and buoy-measured wave direction under different rainfall intensities. 37

2.20 Scatter plots of radar-derived wave period with the sub-image selection scheme and buoy-measured wave period under (a) rainless conditions, (b) light rain conditions, (c) moderate rain conditions, and (d) heavy rain conditions. . . . 39

2.21 Scatter plots of radar-derived wave period without the sub-image selection scheme and buoy-measured wave period under (a) rainless conditions, (b) light rain conditions, (c) moderate rain conditions, and (d) heavy rain conditions. 40

3.1 The route of the vessel during radar data collection periods. 45

3.2 The selected sub-image (outlined in blue) for calculating SNR. 46

3.3 The selected sub-image (outlined in blue) for EEMD-based feature extraction. 48

3.4 Median value distribution of mean of (a) contrast, (b) homogeneity, (c) correlation, and (d) energy. 50

3.5 Median value distribution of standard deviation of the (a) contrast, (b) homogeneity, (c) correlation, and (d) energy. 51

3.6 The overall framework of the TCN-based H_s estimation model. 52

3.7 Visualization of dilated convolution in 6 DCC layers. 53

3.8 The structure of each DCC layer. 54

3.9 A figure illustration of 8 3×1 filters used in the convolution operation. . . . 54

3.10 Scatter plots of buoy-measured H_s and radar-derived H_s with and without temporal moving average. (a), (b), (c), (d), and (e) correspond to SNR-based linear fitting, EEMD-based linear fitting, SVR-based and GRU-based, and the proposed TCN-based methods, respectively. 59

3.11 H_s estimation results in time series using different methods. Cyan and red scatters represent testing samples without and with temporal averaging, respectively. (a), (b), (c), (d), and (e) correspond to SNR-based linear fitting, EEMD-based linear fitting, SVR-based and GRU-based, and the proposed TCN-based methods, respectively. 60

List of symbols

H_s	significant wave height (p.4)
L	size of sliding window (p. 16)
$P^d_\Delta(i,j)$	element in GLCM (p. 17)
Con_Δ	contrast of GLCM in each direction (p. 17)
H_Δ	homogeneity of GLCM in each direction (p. 18)
Cor_Δ	correlation of GLCM in each direction (p. 18)
E_Δ	energy of GLCM in each direction (p. 18)
μ	mean of GLCM (p. 18)
σ	standard deviation of GLCM (p. 18)
P	size of sub-image used for GLCM extraction (p. 19)
W	number of sliding windows in each sub-image (p. 19)
D_i	number of training subset for random-forest based classification method (p. 19)
$I(x,y)$	pixel intensity at location (x,y) in the edge image (p. 21)
δ	Dirac delta function (p. 21)
r	distance from the center of edge image to a candidate straight line in the image (p. 21)
α	projection direction (p. 21)
$f(r,\alpha)$	result of RT (p. 21)
η	texture dominant direction (p. 21)
l	size of edge image (p. 23)

ϕ	rough estimation direction (p. 24)
γ	final texture dominant direction (p. 24)
β	final dominant wave direction of the valid sub-image after true North correction (p. 24)
θ	final estimated wave direction after true North correction (p. 25)
$F_I(\boldsymbol{k}, \omega)$	three-dimensional (3D) image spectrum (p. 46)
$\boldsymbol{k} = (k_x, k_y)$	two-dimensional wave number vector (p. 46)
ω	angular frequency of the ocean wave (p. 46)
g	gravitational acceleration (p. 46)
$\boldsymbol{U} = (U_x, U_y)$	velocity of encounter (p. 46)
q	order of the q^{th}-harmonic (p. 46)
$F_F(\boldsymbol{k}, \omega)$	wave-related image spectrum (p. 47)
$F_H(\boldsymbol{k}, \omega)$	high harmonic spectrum (p. 47)
$F_{BGN}(\boldsymbol{k}, \omega)$	background spectral noise (BGN) spectrum (p. 47)
$F_W(\boldsymbol{k}, \omega)$	wave spectrum (p. 47)
$T_M(\boldsymbol{k})$	empirical modulation transfer function (p. 47)
SNR	signal-to-ratio of a radar image sequence (p. 47)
I_{sub}	sub-image with M rows and N columns for EEMD (p. 48)
$\sum_{j=1}^{5} C_j(\sim, n)$	j^{th} intrinsic mode function (IMF) of the n^{th} column of I_{sub} (p. 48)
$R(\sim, n)$	residual term of the n^{th} column of I_{sub} (p. 48)
$A_j(\sim, n)$	amplitude modulation (AM) part of IMF (p. 49)
S	average of AM portions of 2-5 IMFs (p. 49)
T_{norm}	collection of each type of normalized features (p. 51)
d_n	dilation factor of the n^{th} layer (p. 53)
k	filter size in each convolution operation (p. 53)
$\boldsymbol{x}_{t_0}$	8D feature vectors of sample at the certain time t_0 (p. 54)
$\boldsymbol{y}_{t_0}$	8D result from 6 dilated causal convolution (DCC) layers (p. 54)
f_{ij}	element in filter (p. 54)

$\boldsymbol{t}$	corresponding time of input samples (p. 55)
$\boldsymbol{C}_{\boldsymbol{t}}^{n}$	input of convolution operation at time $\boldsymbol{t}$ in the n^{th} DCC layer (p. 55)
$\boldsymbol{F}_{1}^{n}(\boldsymbol{t})$	output of convolution operation at time $\boldsymbol{t}$ in the n^{th} DCC layer (p. 55)
$\boldsymbol{F}_{2}^{n}(\boldsymbol{t})$	output of ReLU activation function (p. 55)
$\boldsymbol{F}_{3}^{n}(\boldsymbol{t})$	output of the dropout operation (p. 55)
$\boldsymbol{M}$	Bernoulli function (p. 56)
$\boldsymbol{C}_{\boldsymbol{t}}^{n+1}$	output of ReLU after the residual connection (p. 56)
H_{est}	final estimated H_s (p. 56)
w_i	updated weight value (p. 56)
b_i	updated bias (p. 56)

List of abbreviations

UAV	Unmanned Aerial Vehicles (p. 1)
SAR	Synthetic Aperture Radar (p. 1)
HF	High Frequency (p. 1)
2D	Two Dimensional (p. 3)
3D	Three Dimensional (p. 3)
WaMoS II	Wave and surface current monitoring system (p. 3)
FFT	Fast Fourier Transform (p. 3)
MTF	Modulation Transfer Function (p. 4)
SNR	Signal-to-Noise Ratio (p. 4)
BGN	Background Spectral Noise (p. 4)
ILS	Intensity Level Selection (p. 4)
ARPM	Adaptive Recursive Positioning Method (p. 4)
CWT	Continuous Wavelet Transform (p. 5)
RT	Radon transform (p. 5)
EOF	Empirical Orthogonal Function (p. 5)
EEMD	Ensemble Empirical Mode Decomposition (p. 5)
ML	Machine Learning (p. 6)
SVR	Support Vector Regression (SVR) (p. 6)
ANN	Artificial Neural Network (p. 6)
MLP	Multilayer Perceptrons (p. 6)
CNN	Convolutional Neural Network (p. 6)

CGRU	Convolutional Gated Recurrent Unit Network (p. 7)
ZPP	Zero Pixel Percentage (p. 7)
SVM	Support Vector Machine (p. 7)
TCN	Temporal Convolutional Network (p. 9)
GLCM	Gray Level Co-occurrence Matrix (p. 16)
CART	Classification and Regression Tree (p. 20)
MANOBS	Manual of Surface Weather Observations (p. 26)
RMSE	Root-Mean-Square Error (p. 36)
CC	Correlation Coefficient (p. 38)
HH	Horizontal Transmit and Horizontal Receive (p. 44)
IMF	Intrinsic Mode Function (p. 48)
AM	Amplitude Modulation (p. 48)
FM	Frequency Modulation (p. 48)
DCC	Dilated Causal Convolution (p. 52)
ReLU	Rectified Linear Unit (p. 54)

Chapter 1

Introduction

1.1 Research Rationale

Accurate measurement of sea surface wave parameters is critical for a variety of maritime applications, such as offshore wind farm development, oil and gas exploitation, ship navigation, breakwater construction, and cross-sea bridge building [2]. Traditionally, *in situ* sensors such as wave buoys are employed for wave measurements. However, they only provide the sea surface parameters at the current position of interest [3]. In contrast, remote sensing instruments are able to explore and measure sea surface within a much wider area. Remote sensing equipment can be deployed on different platforms, such as satellites, aircraft, low-altitude unmanned aerial vehicles (UAVs), and terrestrial platforms [4]. In recent decades, different remote sensing techniques, e.g., the satellite-borne Synthetic Aperture Radar (SAR) [5], high frequency (HF) radar [6, 7], and X-band marine radar [8] have been utilized to estimate the sea surface wave information. Typical satellite-borne SAR systems lack high temporal resolution because the time interval of revisiting the same location is on the order of days [9]. On the other hand, although HF radar can monitor sea surface parameter for a long distance, spatial resolution of the HF radar is not relatively high since HF radar is operated in the 3-30 MHz frequency range [10]. Among different types of

radar sensors, the X-band marine radar is a favorable choice for real-time wave estimations. Firstly, it has a high temporal resolution [11] since its interval of monitoring is in order of seconds. Also, it has a relatively high resolution to produce finer sea surface parameters. Additionally, compared to SAR, the instruments of X-band marine radar have relatively low installation and maintenance cost [12]. Moreover, X-band marine radar can not only be installed on a fixed offshore platform or nautical traffic control tower but also be mounted on a moving ship to obtain the information of sea surface far from shore [13]. However, the accuracy of sea surface parameters estimated from X-band radar data drops under rain conditions since X-band radar signal is sensitive to rain.

Traditionally, X-band marine radar is used for target detection. In recent decades, it has been found that X-band marine radar may be used as an alternative choice for obtaining sea surface information. The Bragg resonance interactions between the X-band electromagnetic waves and the cm-scale capillary waves induced by local winds generate the radar backscatter from the sea surface [8]. The short waves are then modulated by longer ocean waves under multiple mechanisms such as hydrodynamic effects, tilt modulation, and shadowing effects [2]. Because of this modulation, longer sea surface waves become visible in radar backscatter (i.e., sea clutter) images, which are manifested by strip-like patterns. Although the sea clutter is undesirable for navigation purposes, sea surface variations can be reflected from the sea clutter [14]. Thus, it is possible to utilize the marine radar images to efficiently estimate the sea surface features, such as wind [15, 16] and wave [8, 17–19] parameters.

However, the presence of rainfall will negatively influence the measurement accuracy of those sea state parameters because the raindrops on the ocean surface and in the atmosphere alter both sea surface roughness and X-band radar backscatter [20,21]. Consequently, some wave signatures of radar backscatter images are blurred and existing methods for sea parameter estimation do not work well [13, 22].

1.2 Literature Review

The X-band marine radar operating at grazing incidence is widely applied for the measurements of sea surface parameters. The transmit frequency is from 8 to 12 GHz, and the corresponding radio wavelength is from 2.5 cm to 3.75 cm. The electromagnetic signal transmitted from X-band radar will interact with the rough sea surface. Then, the received backscatter signal was sent to the processor and transformed into radar image so that it can be easily interpreted and studied by the user. During the past several decades, different methods have been proposed for estimating wave information from X-band radar images. In 1966, Wright proposed that sea clutter could be used to obtain the backscattering from capillary waves [23]. In the early research for wave parameter estimation, the methods used were relatively primitive. For example, wave direction could only be measured by the protractor from wave trains in the radar images projected on the screen, and it was also feasible to estimate the wave period from radar images [24]. In the 1980s, spectral-based methods were introduced to analyze the wave information. It was found that two-dimensional (2D) spectra of radar images similar to the spectra derived from buoy data could be obtained by the application of a 2D Fourier transform [25]. However, a directional ambiguity of 180° exists when estimating the wave direction by 2D image spectra. A wave direction ambiguity removal method was proposed in [26], which implemented two sequential images for analysis and combined them with the theory of dispersion for gravity waves. In 1985, a three dimensional (3D) fast Fourier transform (FFT) was applied to a full time series of digitized radar images by Young [8], which could effectively eliminate the 180° directional ambiguity by the introduction of time as the third dimension. In this method, the spatial and temporal features of sea surface from radar data could be combined to analyze the directional wave spectrum. In the two decades following Young's work, the spectral-analysis technique was widely used for sea surface parameter estimation, and it was also integrated into the commercial wave and surface current monitoring system (WaMoS II) [27]. The first step of this method is to transform radar data into the spectral domain by the 3D-FFT to obtain the image spectrum [11]. Then, the surface current can be estimated by least square fitting with

the dispersion relation, which is considered as a band-pass filter to filter the components in the image spectrum that do not belong to the wave field [8]. Eventually, the wave spectrum can be extracted from the wave-related image spectrum by the means of a modulation transfer function (MTF) [11]. Therefore, the wave direction and wave period can be determined from the wave spectrum [28, 29]. However, the wave height cannot be determined directly from the wave spectrum since the intensity of a radar image is directly associated with the strength of radar backscatter signals rather than the sea surface elevation. In the early studies, significant wave height (H_s) was derived from SAR images [30, 31], where it was found H_s was proportional to the square root of the signal-to-noise ratio (SNR) [32]. In subsequent research, the main spectral components from the X-band radar image spectra were analyzed, which include wave components within the dispersion relation shell [8], higher harmonics [18, 33], subharmonic [34], and background spectral noise (BGN) [18, 28]. In 2008, Nieto-Borge *et al.* [18] proposed the SNR-analysis based method to estimate H_s from X-band radar images, and this became one of the most popular methods for H_s estimation. Although the SNR-based method has been incorporated into several commercial radar systems for real-time wave monitoring, later studies have found that H_s is not completely linearly proportional to the square root of SNR since the variations of sea states, the difference in SNR calculation methods and different radar systems will affect the accuracy of the regression model [3, 35, 36].

Several other spectral analysis-based algorithms were presented for wave height estimation after the SNR-analysis based method. In 2014, an iterative least squares (ILS)-based algorithm was proposed to simplify obtaining wave parameters [37] by not requiring a band-pass filter as in the traditional 3D-FFT-based algorithm. A year after, an adaptive recursive positioning method (ARPM)-based algorithm was proposed which could be used to further improve the wave direction and period [38]. However, this technique requires a full radar field of view; otherwise, the estimation accuracy will be affected because of the obstruction of land areas or islands. Wang *et al.* [39] proposed a method to calculate the SNR based on the geometry of the linear wave dispersion relationship, which avoided the problem of

inaccurate surface current measurement. Additionally, it was found that 2-D continuous wavelet transform (CWT)-based algorithms could also be implemented to obtain the wave spectra [40]. In 2017, the array-beamforming based algorithms [41] were proposed to extract the directional wave spectrum and related wave parameters, where beamforming is a technique that extracts the signal arriving from a desired direction through constructive interference and suppresses other signals through destructive interference [42].

Another H_s estimation method is based on texture analysis of X-band radar images. In 1997, Buckley *et al.* [43, 44] proposed that the crest-to-trough length ratio and a threshold probability of illumination could produce a model related to H_s. In 2000, a statistical-analysis-based method was proposed by Gangeskar to determine H_s [45], and an adaptive method was also applied to the problematic situations, such as low wave height and rain condition [46]. In 2005, an algorithm based on tilt modulation was proposed by Dankert to determine the sea elevations [47]. The advantage of this method is that the outputs do not require calibration from an additional reference. Additionally, the Radon transform (RT) was applied for wave direction and wave period estimation by the analysis of wave signatures from X-band radar images [17, 48]. In 2014, Gangeskar [49] conducted a shadowing-analysis-based method to obtain the H_s, which did not require calibration. However, the experimental results needed to be verified by using a usual marine radar installed at a height of 20–30 m since the antenna height of the radar used in that study was much higher (i.e., 43.2 m). Two years later, Liu *et al.* [14] improved the original shadowing-based method by smoothing the edge pixel intensity and extracting a suitable sub-image for analysis. Also, Wei *et al.* [35] considered the water depth effect to the coastal area application based on the shadowing-based method. In 2017, an empirical orthogonal function (EOF)-based method [50] was proposed for the estimation of wave parameters. In this algorithm, H_s, wave period, and wave direction could be determined from the principal components obtained from the EOF. Subsequently, an ensemble empirical mode decomposition (EEMD)-based algorithm was proposed by Liu *et al.* [36], which analyzed the linear relationship between H_s and the parameter derived from EEMD-based method.

Furthermore, it should be noted that in recent years, machine learning (ML)-based algorithms have been increasingly incorporated into wave parameter estimation models. Firstly, support vector regression (SVR) is an appealing algorithm for a large variety of regression problems, which does not only consider the error approximation to the data, but also the generalization of the model. In 2015, Salcedo-Sanz *et al.* [51] extracted the probability of shadowing and tangent of the local incidence angle as input variables from the simulation-based data to obtain H_s using the SVR-based method. In the following year, Cornejo-Bueno *et al.* [52] extracted SNR, peak wave number and peak frequency derived from the wave number spectrum, and different estimations of the mean powers of the frequency derived from the ratios of the spectral moments. Then, these parameters were used as predictive variables to train the SVR-based H_s estimation model. In addition, the artificial neural network (ANN) is also a ML-based regression algorithm often used to estimate H_s. In 2012, Vicen-Bueno *et al.* [53] extracted $\sqrt{\text{SNR}}$ from the consecutive radar image sequences, wave period, and wave length as inputs to estimate H_s by using a non-linear ANN model with multilayer perceptrons (MLP). The introduction of multiple parameters for H_s analysis can mitigate the H_s overestimation problem under low wind speeds. In 2020, Park *et al.* [54] also applied the ANN-based method with $\sqrt{\text{SNR}}$, wave period, and wind condition parameters to estimate H_s. In 2021, the ANN-based regression model was also used to analyze the influence of non-onshore winds on H_s from the off-shore X-band radar system [3]. In addition to $\sqrt{\text{SNR}}$, the powers from nearshore radar subimages and *in situ* wind components were also included as input parameters of the neural network to improve the H_s estimations from coastal radar images. It can be found the SVR-based methods and the ANN-based method use the square root of SNR as the main feature to train the estimation model. Thus, it is worthwhile that more effective features are combined for analysis to improve the estimation accuracy.

In the past two years, more advanced neural networks have been applied to sea parameter estimation. For example, in 2020, a convolutional neural networks (CNN)-based regression method was proposed to obtain the wave period and H_s from the sub-images extracted

from simulated X-band radar images [55]. However, the validation of the method was based on a simulated image data set and requires further validation for real data. In 2021, a convolutional gated recurrent unit network (CGRU) was used to estimate H_s by Chen *et al.* [13], which effectively took into account the temporal features of the radar image time series. However, both deep learning-based methods use the radar images instead of features extracted from the images as input directly to train the estimation model. This end-to-end system cannot reflect the mapping relationship between the features and wave parameters.

In most of the above-mentioned parameter estimation techniques only radar images collected under rain-free conditions were used. This is due to the known fact that those techniques yield significantly decreased estimation accuracies when applied to rain-contaminated radar images. In order to detect the presence of rain from radar images, a variety of methods have been proposed to classify the radar images into rainless and rain-contaminated types, including the mean-and-difference-coefficient-analysis based method [56], zero-pixel-percentage (ZPP) based method [15], and the support-vector-machine (SVM) based method [57]. Besides those, a couple of modified and novel methods for wind parameters estimation with rain mitigation have been proposed, such as the modified-intensity-level-selection based method [58], the EEMD-based method [59], and the SVR-based method [60]. In contrast, few studies have been conducted for wave parameter estimation using rain-contaminated radar images. In 2012, rain-contaminated radar images could be identified by analyzing the change trend of the 3D evaluation parameters of surface roughness of radar images and SNR [56]. It was found that in the wave spectrum of radar image sequences not seriously affected by rain, the energy in low frequency part is higher than that of rainless radar image sequences. Therefore, those radar images which were not seriously affected by rain could be selected by comparing the energy difference in low frequency part of the wave spectrum and then filtered in frequency domain to improve the estimation accuracy of wave period and wave direction. In 2017, a rain influence correction method on the gray level radar image based on 1-D complex continuous wavelet transform was proposed [61]. In 2021, the proposed CGRU-based method would also improve the H_s estimation accuracy under rain

condition [13].

1.3 Motivation and Objectives

Although some algorithms mentioned above for estimating wave parameters under rain condition have been proposed, it is found that the influence of rainfall intensity on wave parameter estimation accuracy has never been analyzed. Thus, it is worthwhile to estimate the wave period and direction under different rainfall intensities. On the other hand, these existing studies for rain radar data just utilize preliminary methods for analysis, which still have some shortcomings to be improved. For example, those radar images severely contaminated by rain are not available for wave period and direction estimation when using the method proposed in [56]. Although the 1-D complex continuous wavelet transform-based method [61] can correct the rain-contaminated radar image to some extent, the correction performance does not work well for those regions where the wave signatures are completely blurred by rain. According to Huang *et al.* [62], for rain-contaminated images, regions that are unaffected or less affected by rainfall can still be used to estimate sea surface parameters. Thus, it is necessary to develop a novel scheme to identify and select regions with clear wave signatures for wave parameter estimation. Therefore, the objective of the first part in this thesis is to evaluate the influence of different rainfall intensities on the measurement of wave direction and period as well as mitigate the rain effect on the wave direction and wave period estimation.

As for the H_s estimation, it is found that traditional SNR-based linear fitting method cannot effectively produce accurate results, especially when radar data are collected from a moving platform [36]. Besides, those calibration-free methods, such as shadowing-analysis-based [49] and EOF-based [50] methods are composed of more complicated structures and computation steps than that of using calibration reference methods. On the contrary, ML-based methods can simplify the design of algorithms and improve the estimation accuracy

efficiently. For now, some ML-based H_s estimation methods, e.g., CNN-based and CGRU-based methods are end-to-end systems, which can extract features automatically and produce relatively high accuracy. However, it is hard to analyze the relationship between those highly abstract features and H_s. On the other hand, a more advanced ML-based regression method can be developed to improve the estimation accuracy of H_s. Among different types of neural networks, the temporal convolutional network (TCN) is a variant of CNN architecture for sequence network modeling proposed in [63]. Compared to models based on other typical CNNs, TCN-based estimation model can exhibit longer effective memory, which indicates that H_s can be analyzed in conjunction with more long-term data. Thus, H_s can not only be estimated from the spatial features extracted from the current radar image, but also the temporal variations exploited from preceding radar image sequence. Therefore, the second objective is to utilize the state-of-the-art TCN-based regression method to further improve the H_s estimation accuracy from rain-free radar data.

1.4 The Scope of the Thesis

In this thesis, novel algorithms are developed to estimate wave parameters, i.e., wave direction, wave period, and H_s. The thesis is organized as follows:

In Chapter 2, a sub-image selection scheme is proposed to mitigate the rain effect on the rain-contaminated radar images. Then, the wave direction and wave period are estimated based on the RT and random forest regression methods under different rain intensities.

In Chapter 3, a TCN-based regression model is proposed to estimate H_s under rainless conditions.

A summary of the thesis and some suggestions for future work are addressed in Chapter 4.

The achievements of this research have been published in the following journal papers:

1. Z. Yang, W. Huang, and X. Chen, "Evaluation and mitigation of rain effect on wave

direction and period estimation from X-band marine radar images," *IEEE J. Sel. Top. Appl. Earth Obs. Remote Sens.*, vol. 14, pp. 5207–5219, 2021.

2. W. Huang, Z. Yang, and X. Chen, "Wave height estimation from X-band nautical radar images using temporal convolutional network," *IEEE J. Sel. Top. Appl. Earth Obs. Remote Sens.*, vol. 14, pp. 11395–11405, 2021.

Chapter 2

Evaluation and Mitigation of Rain Effect on Wave Direction and Period Estimation from X-band Marine Radar Images

In this chapter, quantitative analysis of the effect of rain intensities on wave direction and period estimation from X-band radar data is presented. A sub-image selection scheme for identifying the region with relatively clear wave signatures to improve the estimation accuracy and a ML-based wave period measurement method are proposed. In Section 2.1, the radar and environmental data used in this study are described. The proposed methodology is illustrated step by step in Section 2.2. Section 2.3 contains the experimental results as well as rain effect analysis. Finally, the chapter summary is addressed in Section 2.4.

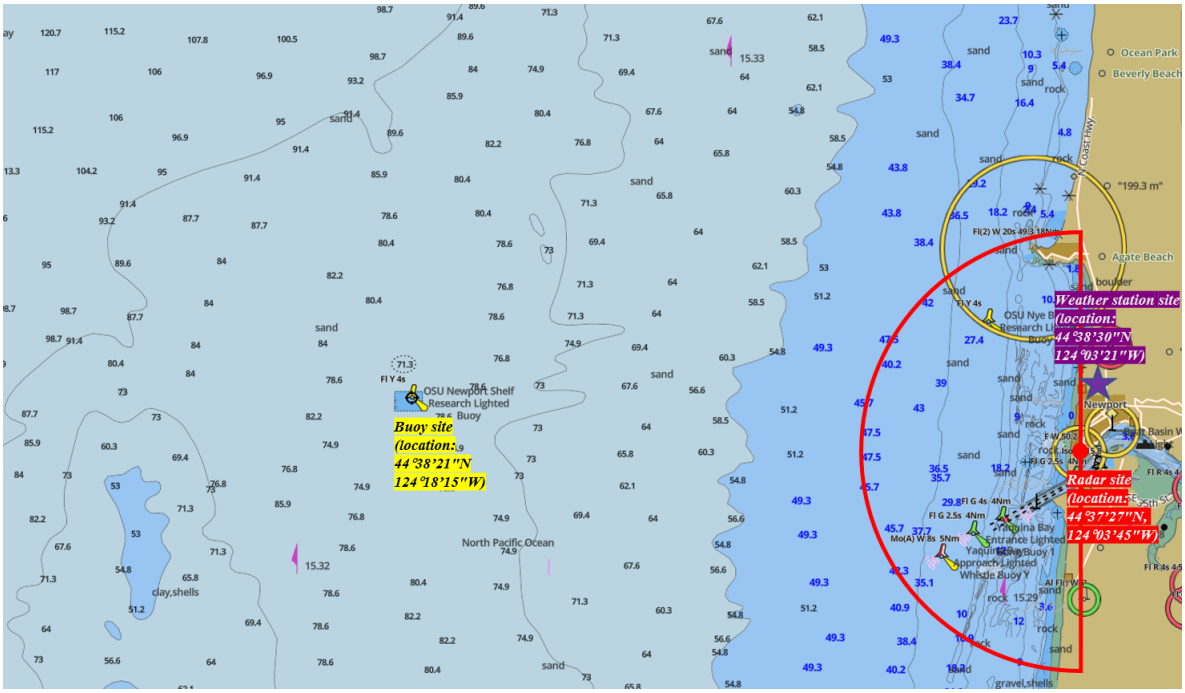

Figure 2.1: Locations of the radar, buoy, and weather station site as well as the bathymetry of the region from GPS Nautical Charts [1].

2.1 Data overview

The radar data used in this study were collected by a commercial X-band marine radar (Koden) deployed on a shore-based tower at Yaquina Bay, Newport, OR, USA (44°37'27"N, 124°03'45"W). The radar system specifications are provided in Table 2.1. The range resolution of this radar is 12 m, and beam width is 0.8°. The resolution of the Cartesian radar image is 5 m. Fig. 2.1 shows the locations of the radar, buoy, and weather station site as well as the bathymetry of the region. The coverage of the radar image is shown by a red sector. According to the bathymetry map, the water depths of the observation area range from 0 to 47.5 m. In this study, regions with water depths shallower than 10 m are excluded from the analysis. This is because that as the deep-water waves travel into shallow water, they will interact with the seabed, resulting in the variations of wave period and direction [64]. The reference wave information is collected per hour by a TriAXYS directional wave buoy located

Table 2.1: Radar information

Radar site	A shore-based tower in Newport, OR, USA
Transmit frequency	9.45 GHz
Polarization	Horizontal
Pulse width	80 ns
Range resolution	12 m
Range coverage	3 m - 6087 m
Beam width	0.8°
Azimuth coverage	180°
Antenna height	63 m
Antenna rotation speed	44 rpm
Grey level of radar image	0 - 255

around 20 kilometers from the radar site (44°38'21"N 124°18'15"W). According to [65], the buoy can measure wave periods of 1.5 s to 30 s with a resolution of 0.1 s. The accuracy of the measured wave period is better than 1%. The buoy measures wave direction from 0° to 360° with a resolution of 1° and the measurement error is within 3°. The hourly average rain rate was recorded every 5 minutes from a rain gauge with a resolution of 0.1 mm/h and provided by the ARPSWXNET/CWOP weather station (44°38'30"N 124°03'21"W). The measurement error is within 0.5 mm/h. The radar, buoy, and rain gauge instruments are all working 24/7. Since the sampling rates of both buoy and rain gauge are lower than that of the radar, the reference wave and rain data for each radar image are obtained from the closest measurements before or after the image acquisition time. The radar images used for this study were selected between January 11 and July 18, 2019 under a wide range of rain rates. Among those images, 70% of them were randomly selected for training while the other 30% were used for testing.

2.2 Methodology

The overall framework of wave direction and period estimation in this study is presented in Fig. 2.2.

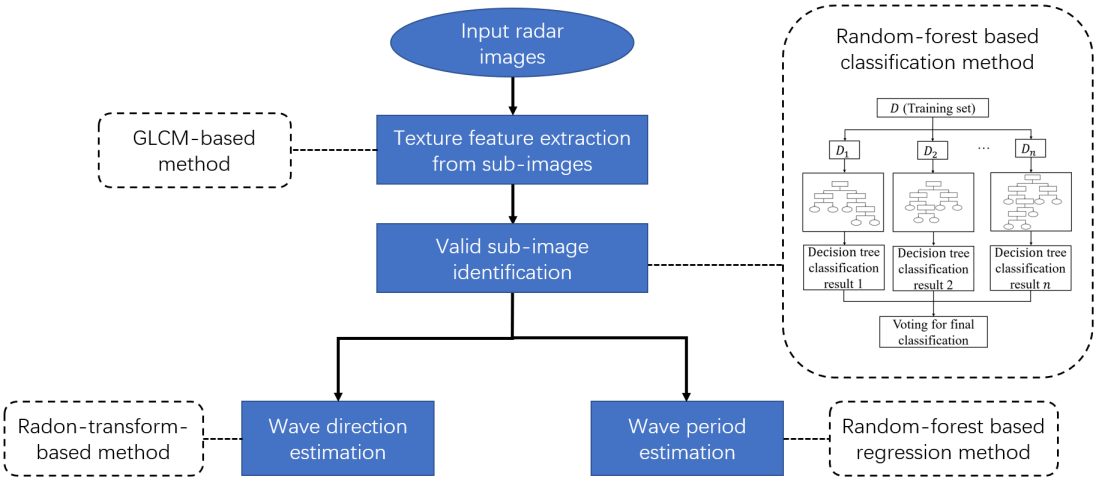

Figure 2.2: Framework of wave direction and period estimation.

2.2.1 Sub-image Selection

Fig. 2.3 shows examples of radar images obtained under four different rainfall intensities. It can be observed that wave signatures will be affected by different degrees under different rain rates. Specifically, a rain-free radar image is presented in Fig. 2.3(a), and the texture of wave signatures can be clearly observed in most of the sea surface regions. In comparison, Figs. 2.3(b), (c), (d) are radar images with blurry wave signatures obtained under rain rates of 1.5 mm/h, 3.0 mm/h, and 9.1 mm/h, respectively. It may be observed that as rain rate increases, the proportion of regions dominated by rain echoes increases as well.

For some rain-contaminated images, wave signatures might still be visible in some regions, from which wave parameters can be estimated [62]. On the other hand, regions dominated by rain echoes should be discarded. In order to identify those regions with visible wave signatures, 15 sub-images with equal size are first extracted from each radar image, as shown in Fig. 2.4. For each sub-image, texture features are extracted and input into a random-forest-based classification model, which is able to determine whether the sub-image is dominated by visible wave signatures (i.e, valid sub-image) or rain-echoes (i.e, invalid sub-image). If all the 15 sub-images in one radar image are identified as invalid sub-images, this radar image will be discarded from wave estimation as well. The detailed procedures

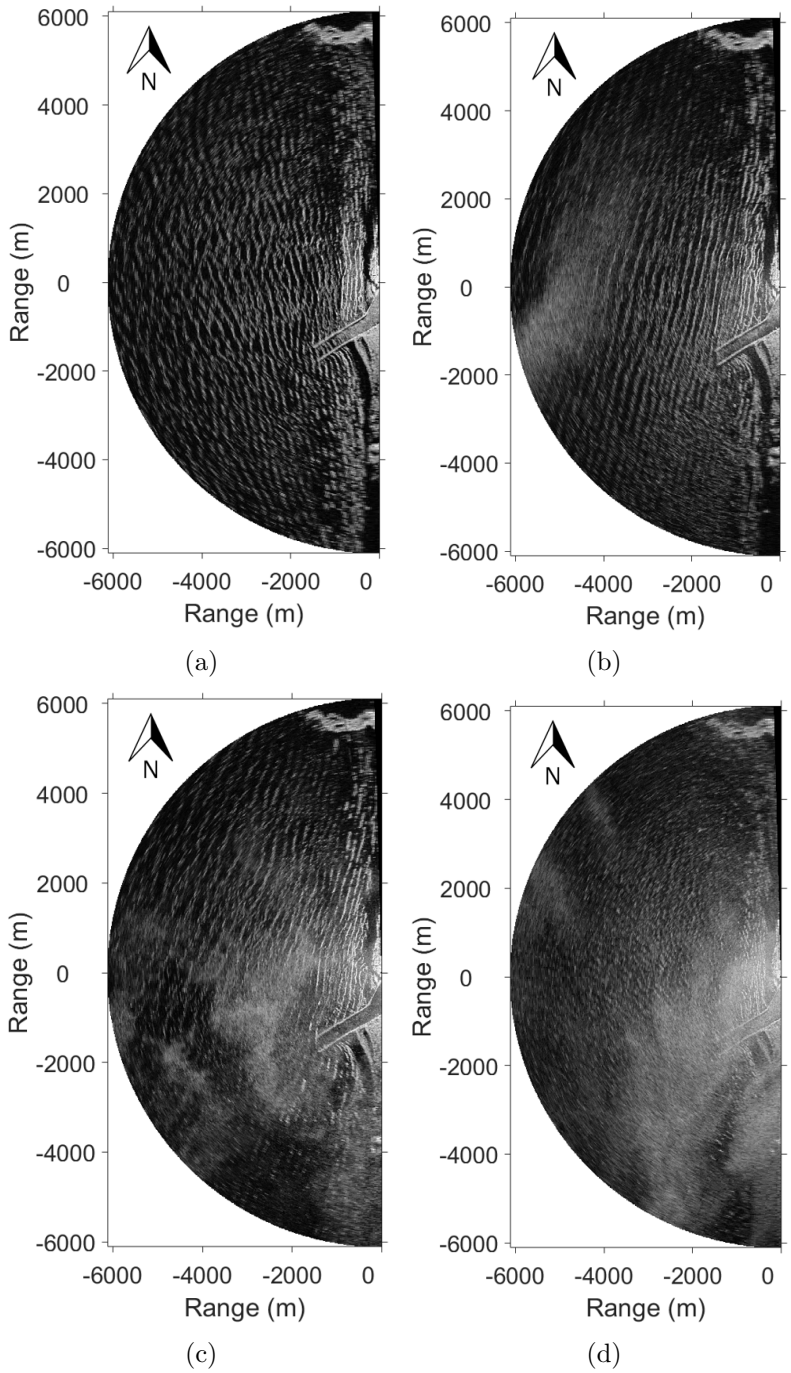

Figure 2.3: Radar images obtained under different simultaneous rainfall intensities: (a) rainless, (b) 1.5 mm/h rain rate, (c) 3.0 mm/h rain rate, (d) 9.1 mm/h rain rate.

for texture feature extraction and sub-image classification are introduced below.

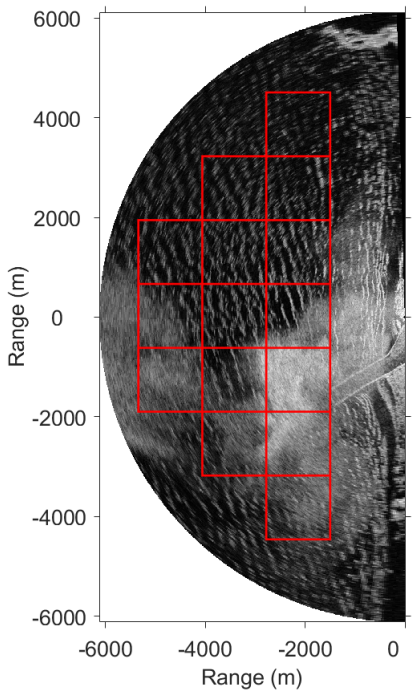

Figure 2.4: Selection of 15 sub-images (outlined in red) in the radar image.

Feature Extraction

The gray level co-occurrence matrix (GLCM)-based method [66] that reflects the correlation characteristic of image grayscale space is an efficient texture analysis approach and used here for feature extraction from each sub-image. Firstly, a $L \times L$ sliding window is applied to the sub-image. In each window, the pixels with the maximum and minimum intensities in the window are set as gray level 15 and gray level 0, respectively. Then, other pixels within the window are scaled to the integers between 0 to 15 based on the min-max feature scaling. The min-max feature scaling can convert the values to a range between 0 and 1 via

$$X' = \frac{X - \min(X)}{\max(X) - \min(X)}, \tag{2.1}$$

where X is the original value and $X^{'}$ is the normalized value. Next, the GLCMs are formed from each pixel-intensity-scaled window as

$$P_{\Delta}^{d} = \begin{bmatrix} P_{\Delta}^{d}(0,0) & P_{\Delta}^{d}(0,1) & \cdots & P_{\Delta}^{d}(0,15) \\ P_{\Delta}^{d}(1,0) & P_{\Delta}^{d}(1,1) & \cdots & P_{\Delta}^{d}(1,15) \\ \vdots & \vdots & \ddots & \vdots \\ P_{\Delta}^{d}(15,0) & P_{\Delta}^{d}(15,1) & \cdots & P_{\Delta}^{d}(15,15) \end{bmatrix} \tag{2.2}$$

The element (denoted as $P_{\Delta}^{d}(i,j)$) of the GLCM indicates the number of occurrences of the pair of pixels which have intensities of i and j $(i,j = 0,1,2...,15)$ with a distance d along direction Δ. The Chebyshev distance, which is used to calculate the distance (d) between two pixel positions (x_1, y_1) and (x_2, y_2) in this study, equals to $\max(\text{abs}(\text{x}_1 - \text{x}_2), \text{abs}(\text{y}_1 - \text{y}_2))$. The directional relationships of pixel pairs are shown in Fig. 2.5 and

- $\Delta = 1$ (in 0^{o} direction);
- $\Delta = 2$ (in 45^{o} direction);
- $\Delta = 3$ (in 90^{o} direction);
- $\Delta = 4$ (in 135^{o} direction).

Since for a certain distance d each direction Δ can be chosen to create one GLCM, four GLCMs can be generated in each sliding window.

Finally, a feature vector is constructed based on the statistics of the GLCMs. In [66], fourteen statistics can be calculated from the GLCM. In this study, four of them, i.e., contrast (denoted as Con), homogeneity (denoted as H), correlation (denoted as Cor), and energy (denoted as E) are selected and calculated for each GLCM, respectively, as

$$Con_{\Delta} = \sum_{i} \sum_{j} (i-j)^2 P_{\Delta}^{d}(i,j), \tag{2.3}$$

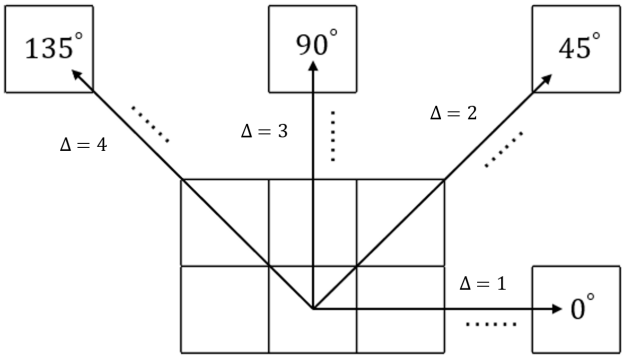

Figure 2.5: The pixel pairs in four directions having the same Chebyshev distance.

$$H_\Delta = \sum_i \sum_j \frac{1}{1+|i-j|} P_\Delta^d(i,j), \tag{2.4}$$

$$Cor_\Delta = \sum_i \sum_j \frac{(i-\mu_i)(j-\mu_j)P_\Delta^d(i,j)}{\sigma_i \sigma_j}, \tag{2.5}$$

where μ and σ are the mean and standard deviation of the GLCM, respectively.

$$\mu_i = \sum_i \sum_j i P_\Delta^d(i,j), \tag{2.6}$$

$$\mu_j = \sum_i \sum_j j P_\Delta^d(i,j), \tag{2.7}$$

$$\sigma_i^2 = \sum_i \sum_j P_\Delta^d(i,j)(i-\mu_i)^2, \tag{2.8}$$

$$\sigma_j^2 = \sum_i \sum_j P_\Delta^d(i,j)(j-\mu_j)^2. \tag{2.9}$$

Also, the energy can be expressed as

$$E_\Delta = \sum_i \sum_j P_\Delta^d(i,j)^2. \tag{2.10}$$

In addition, the mean and standard deviation of each feature are calculated over four directions and composed as an 8-dimensional feature vector for each sliding window. The reason why these features are selected for analysis will be illustrated in Section IV. The size (L) of the sliding window and the distance (d) between pixel pairs along four directions are set as 9 and 1 respectively for the method used in this study. Then, for each sub-image, the 8-dimensional features of all sliding windows are combined together as one feature vector. Thus, in each sub-image ($P \times P$ in pixels), the number of sliding windows (denoted as W) can be calculated as $W = (P - L + 1)^2$. In order to facilitate the computation of feature vectors, all the sub-images are resized into 100×100 pixels using bicubic interpolation [67]. Therefore, 8486 sliding windows can generate a feature vector with 67,712 elements in each sub-image.

Random Forest Classification

After obtaining the texture features for all the sub-images in each image, the random-forest based classification method is used to identify the valid sub-images. Random forest [68] which consists of a large number of decision trees is an ensemble learning algorithm and can be used for both classification (in this section) as well as regression. The ensemble method is a technique that combines the predictions from multiple decision tree models to make more accurate predictions than any individual model. The randomness of the random forest is reflected from selecting a random set of features from all features and random samples from the training dataset for each decision tree.

The architecture of the random forest classifier is shown in the right block diagram in Fig. 2.2, which consists of three steps (i.e., bootstrapping, decision tree training, and prediction). The first is to generate one subset via bootstrapping for each decision tree. Bootstrapping is a sampling method to draw around 63.2% samples randomly from the training set (i.e., D in Fig. 2.2) with replacement as the training subset for the decision tree [69]. Usually, a total of n training subsets (i.e., D_1, D_2, ..., D_n in Fig. 2.2) should be generated (i.e., n sampling times). As for the training set, all sub-images from 90 radar

images obtained under different rainfall intensities are first manually labelled into two types: those with relatively clear wave signatures and those without clear wave signatures. Then, the extracted feature vectors of these labelled sub-images and their corresponding labels are combined as the training set, while the remaining radar images are used as the testing set. The involvement of many decision trees can reduce the variance efficiently, avoid overfitting, and improve generalization. Therefore, the number of sampling times is chosen as 100 (i.e., 100 subsets or decision trees).

Next, each training subset is employed to train one decision tree model based on the Classification and Regression Tree (CART) method [70] which is able to predict classification results according to the feature differences of the input training set. In each decision tree training, the square root of the number of all features is considered as the number of selected random features which are used for decision node selection [68]. The purpose of selecting a random set of features is to reduce the correlation between each decision tree and improve the classification accuracy of each decision tree. Additionally, the selection of the optimal feature as a decision node can be referred to as the CART method [70]. After obtaining each decision tree model, every individual tree in the random forest will produce a class prediction result. Thus, each testing sample in the testing set is input into each decision tree model, and a total of 100 classification results will be generated here. Then, a majority voting scheme is applied, which means that the class with the most votes according to all decision trees' prediction results becomes the random forest classification model's final prediction.

The valid wave regions of each radar image can be obtained using the classification method and used for wave parameter measurement. The framed red boxes in Fig. 2.6 are the valid sub-images identified from the rain-contaminated radar image in Fig. 2.4.

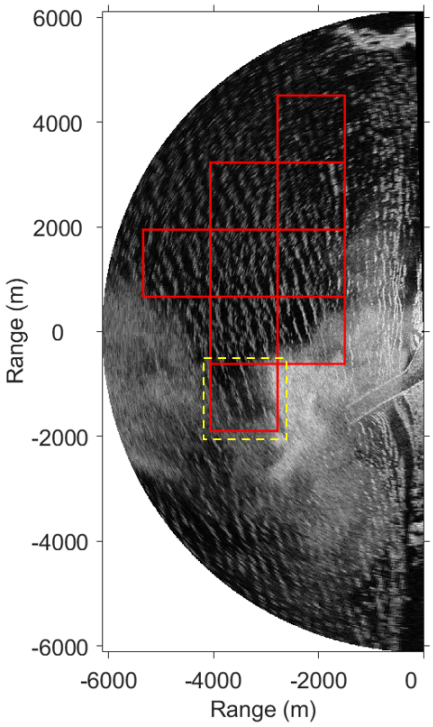

Figure 2.6: Valid sub-images (outlined in red) identified from radar image in Fig. 2.4.

2.2.2 Wave Direction Estimation

After obtaining the valid sub-images for each radar image, the classic method for edge detection, i.e., Canny edge detection proposed in [71], is first performed on each valid sub-image in order to facilitate line detection using the RT in the next step. In this study, in order to outline the main texture with lower computation load, each sub-image used for edge detection is still 100×100 pixels. An example of the edge detection result of a valid sub-image (i.e, Fig. 2.7(a)) is presented in Fig. 2.7(b). Next, the dominant direction (denoted as η) of each edge image is estimated using the RT-based method. The RT [72] can be expressed as

$$f(r, \alpha) = \int \int I(x, y)\delta(r - x\cos\alpha - y\sin\alpha)dxdy, \tag{2.11}$$

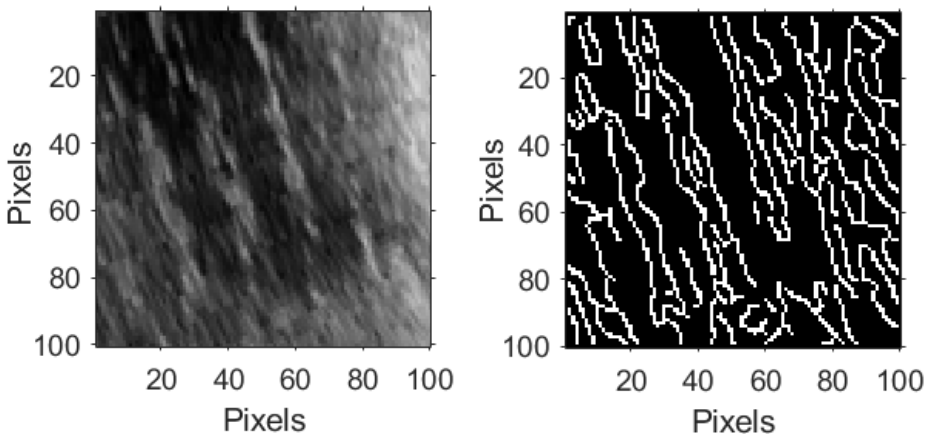

(a) (b)

Figure 2.7: (a) The valid sub-image highlighted in yellow dash lines in Fig. 2.6. (b) The detected edge image of (a).

where $I(x, y)$ is the pixel intensity at location (x, y) in the edge image, δ is the Dirac delta function, r represents the distance from the center of the edge image to a candidate straight line in the image, and α is the angle between the normal of the straight line and x-axis, which is also the projection direction of the straight line. It is obvious that only the line

$$r = x \cos \alpha + y \sin \alpha, \tag{2.12}$$

contributes to the integral in Eq. (2.11). The α and r in Eq. (2.11) represents the integral of the intensity of all the pixels on a line which is in the direction α and at a distance r relative to the image center, i.e., each point in the RT domain corresponds to a straight line in image space. As for the detected edge image, it can be found that one texture line with high gray level and a distance r as well as direction α relative to the edge image center will generate a bright point at (α, r) in the RT domain. On the contrary, the texture line with low gray level will generate a dark point in the RT domain. Thus, the pixels in the RT domain image in the corresponding texture line projection direction will display the largest intensity value variation. The standard deviation of the pixel intensities in each projection direction (α) of the transformed result in the Radon domain can be calculated, and the

direction with the peak standard deviation value can be considered as the texture dominant direction (η).

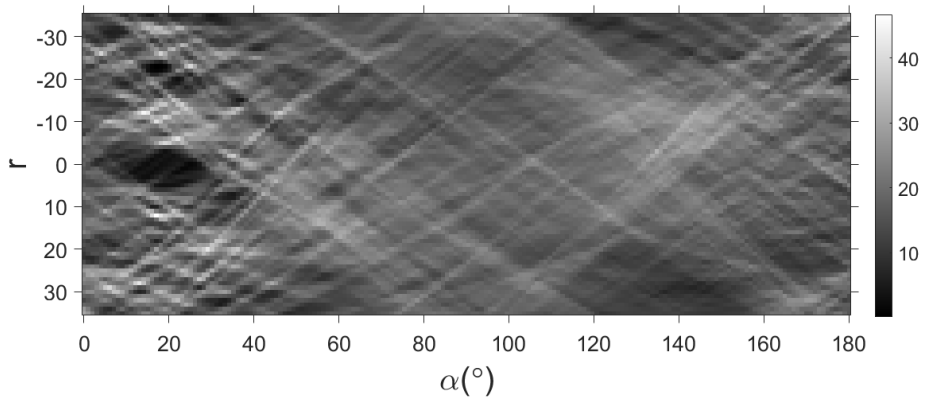

(a)

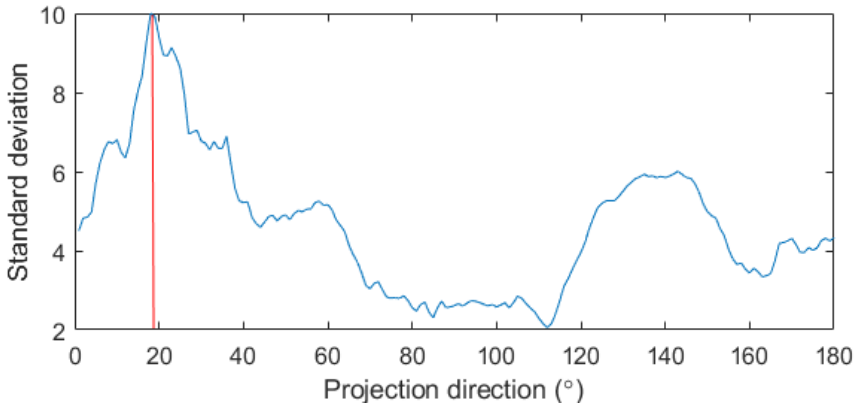

(b)

Figure 2.8: (a) The RT results of all projection lines in Fig. 2.7(b). (b) The standard deviation of RT results as a function of projection direction.

To reduce computation, for an edge image which contains l pixels on each side, only the projection lines that have at least $l/\sqrt{2}$ pixels are used for the RT, which means the absolute value of applicable distance r is less than $l/(2\sqrt{2})$ pixels. Based on this criterion, the RT result of Fig. 2.7(b) is presented in Fig. 2.8(a). Besides, the standard deviation of the pixel intensities in each projection direction (α) of Fig. 2.8(a) is calculated and shown in Fig. 2.8(b). It can be observed that the texture dominant direction of Fig. 2.7(a) is 18°. Furthermore, for each radar image, the standard deviations of RT results obtained from

all valid sub-images are averaged for each projection direction, and the direction with the maximum averaged standard deviation is selected as a rough estimation direction (denoted as ϕ). Next, by comparing η with ϕ, only those sub-images with η being within $\pm 10^{\circ}$ of ϕ are selected, and the median value of η associated with the selected sub-images is regarded as the final texture dominant direction (denoted as γ) of one radar image [17]. It should be noted that η and γ should be converted to β and θ which are measured with reference to the true North.

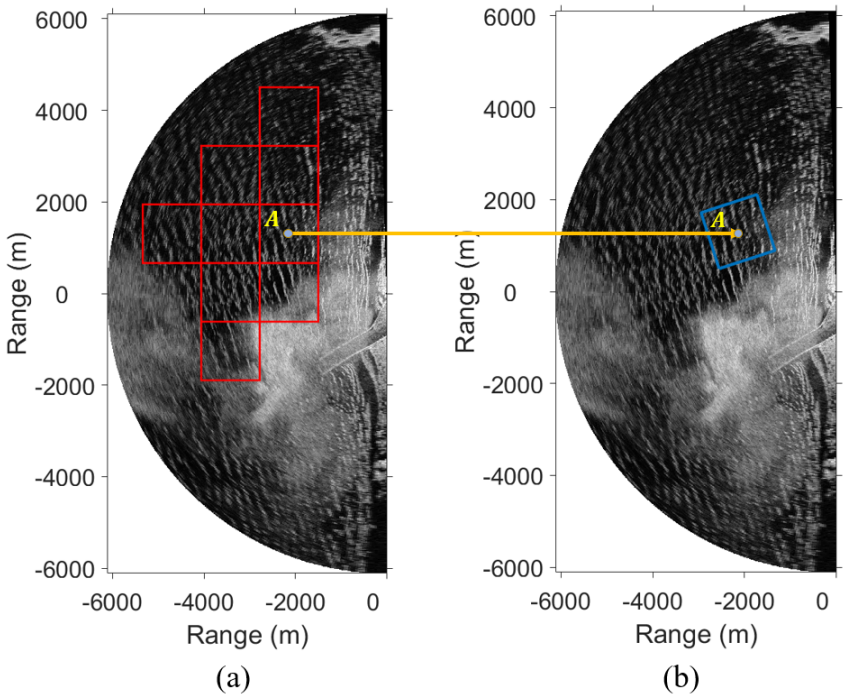

Figure 2.9: The region extraction for wave period estimation. (a) The selected valid sub-image centering at A. (b) The extracted region centering at A for wave period estimation outlined in blue.

2.2.3 Wave Period Estimation

The steps for wave period estimation are illustrated as follows. As shown in Fig. 2.9(a), the valid sub-image with its dominant wave direction (β) closest to the estimated wave direction

(θ) from the corresponding radar image is selected. Then, a 256 $\times$ 256-pixel region (1280 m $\times$ 1280 m) which centers at the original sub-image center with two sides aligning with the estimated wave direction is selected for wave period estimation, as depicted in Fig. 2.9(b). Similar to the sub-image selection step, the GLCM-based method is also used for texture feature extraction. In this method, the size of the sliding window is 59 $\times$ 59 pixels (295 m $\times$ 259 m) and the distance between the pixel pairs is selected as 4. Since the wave period is related to the spacing between the wave signatures [73], if the window size is too small, the sliding window cannot include sufficient wave signatures and therefore cannot reflect accurate spacing between the wave signatures. In contrast, the number of generated texture features would be less if a larger window were used because the number of available sliding windows will decrease. As for the distance between the pixel pairs, the value of 4 is chosen to ensure it is large enough to capture most variations of pixel intensities between adjacent wave crests and troughs. If the distance value is too small, the variations between pixel pairs may not be observed, while a very large distance will cause the fact that the feature obtained does not represent the variation between adjacent wave crests and troughs. Therefore, in each 256 $\times$ 256 sub-image, 39204 sliding windows can generate 313632 feature values to obtain one feature vector.

After obtaining the texture features, the random-forest-based regression algorithm [74] is used to train the wave period estimation model. Although the main training steps of the random-forest-based regression model are the same as those of the aforementioned random-forest classification algorithm, the goal of the proposed regression model is to obtain the smallest difference between the actual data value (buoy-measured wave period in this study) and the radar-derived wave period. Besides, the number of randomly selected features for training of each decision tree is one third of all features [68]. Moreover, the output at each leaf of the decision tree is wave period. In this study, the final predicted wave period of each radar image equals the average of the predicted results generated by 100 trained regression models.

2.3 Experimental Results

In this study, the radar-derived estimation results are analyzed under four rainfall intensity levels, i.e., rainless, light rain, moderate rain, and heavy rain. According to the Manual of Surface Weather Observations (MANOBS) [75], the range of rain rates for each level is

- Rainless: Zero rain rate;
- Light rain: Nonzero rain rates less than 2.5 mm/h;
- Moderate rain: Rain rates between 2.6 to 7.5 mm/h;
- Heavy rain: Rain rates between 7.6 to 50 mm/h.

Also, in order to validate the effectiveness of the sub-image selection scheme for rain effect mitigation, the proposed wave direction and wave period estimation algorithms without applying the sub-image selection scheme are also implemented for comparison. In the latter case, all the 15 sub-images in each radar image are used for wave parameter estimation.

2.3.1 The Influence of Rain on Extracted Features

In order to verify the effectiveness of classifying between rainless and rainy images using these four features (Con, H, Cor, and En) from GLCM, the mean and standard deviation of each feature calculated from rainless and rainy sub-images for different wind speeds, observation ranges, and observation directions are compared with each other with the results being shown in the box plots in Figs. 2.10 to 2.17. In each figure, the red and blue box plots represent the results calculated under rainless and rainy conditions, respectively. From Figs. 2.10-2.13, it can be observed that the medians of mean contrast under rainless conditions are generally lower than those obtained under rainy conditions. In contrast, the medians of mean homogeneity, correlation, and energy under rainless conditions are all larger than those obtained under rainy conditions. From Figs. 2.14-2.17, it may be observed that most of the median standard deviations calculated from the contrast, homogeneity, and energy

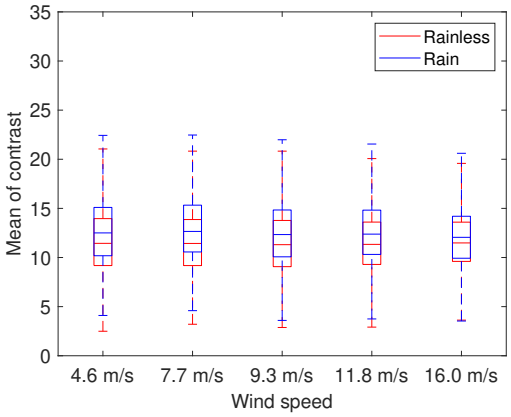

(a)

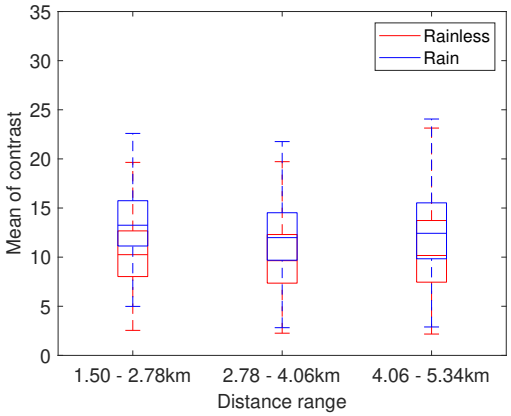

(b)

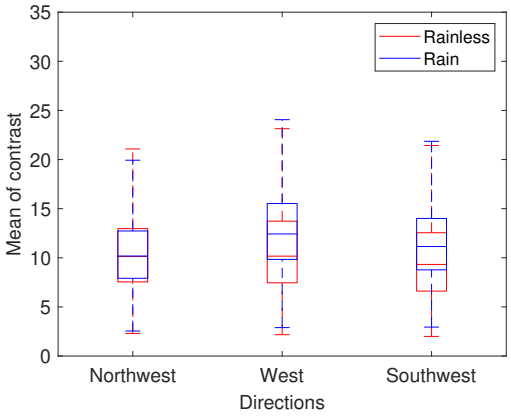

(c)

Figure 2.10: Box plots of the mean contrast distributions for different (a) wind speeds, (b) ranges, and (c) directions.

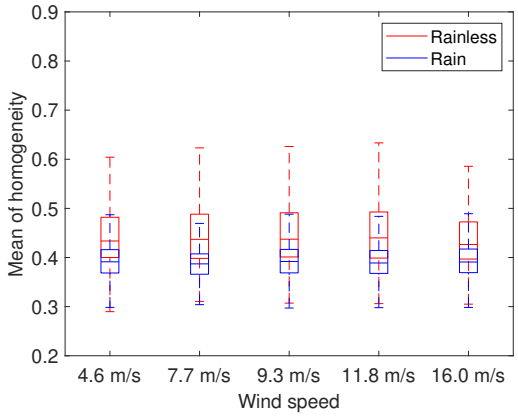

(a)

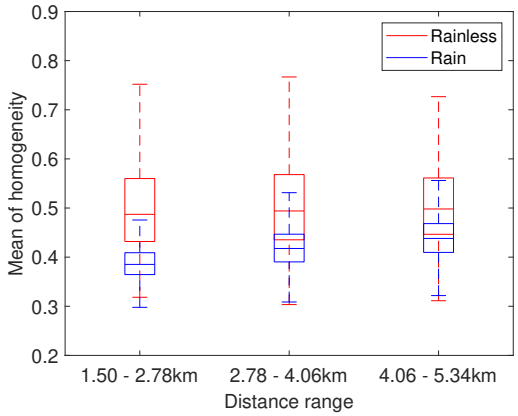

(b)

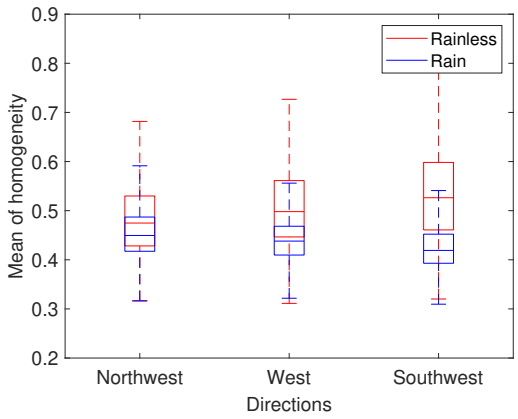

(c)

Figure 2.11: Box plots of the mean homogeneity distributions for different (a) wind speeds, (b) ranges, and (c) directions.

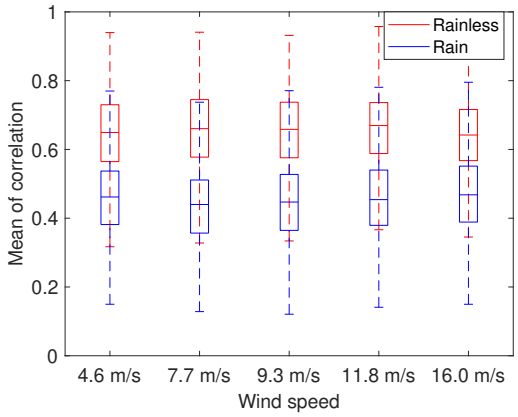

(a)

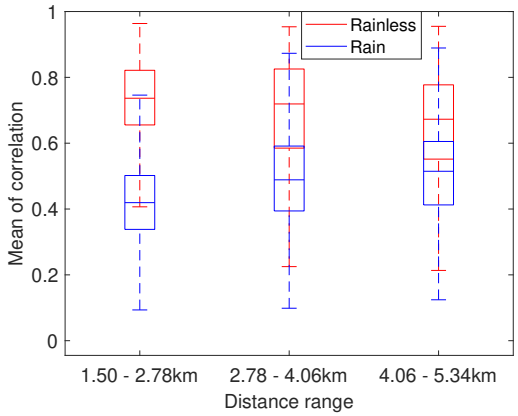

(b)

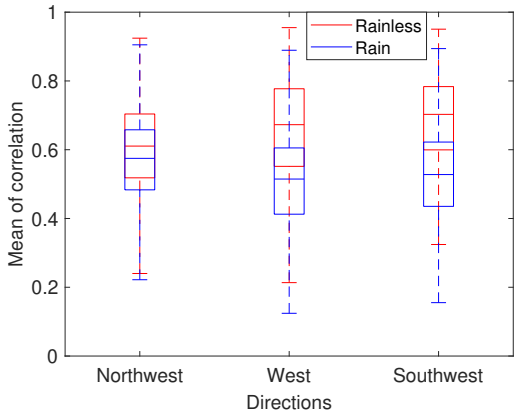

(c)

Figure 2.12: Box plots of the mean correlation distributions for different (a) wind speeds, (b) ranges, and (c) directions.

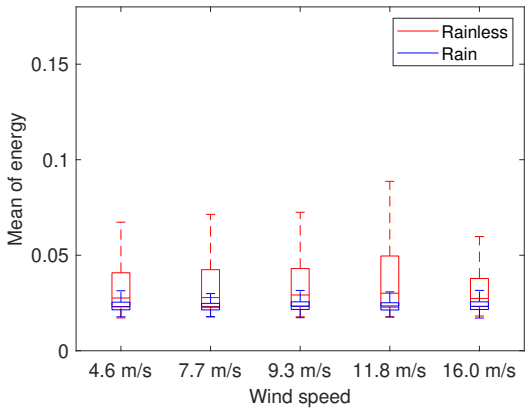

(a)

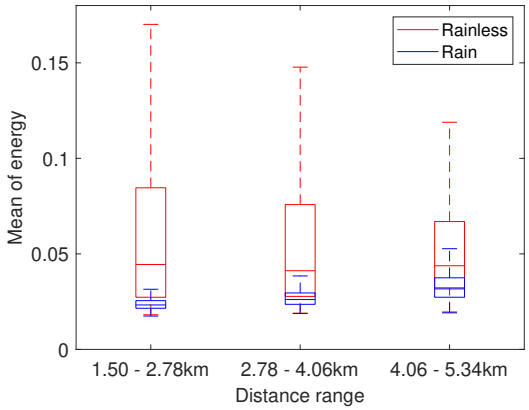

(b)

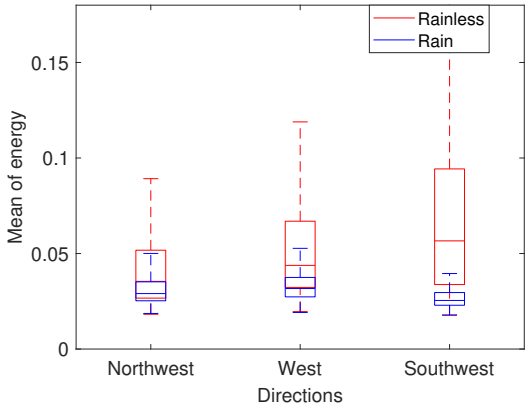

(c)

Figure 2.13: Box plots of the mean energy distributions for different (a) wind speeds, (b) ranges, and (c) directions.

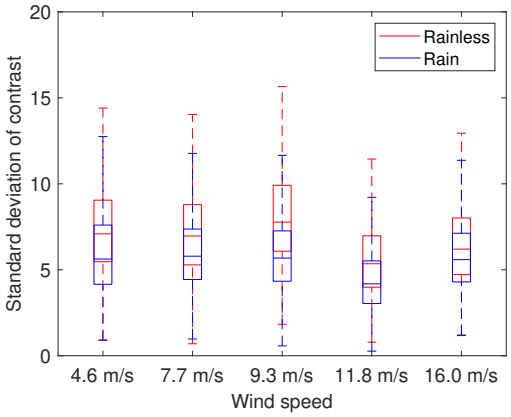

(a)

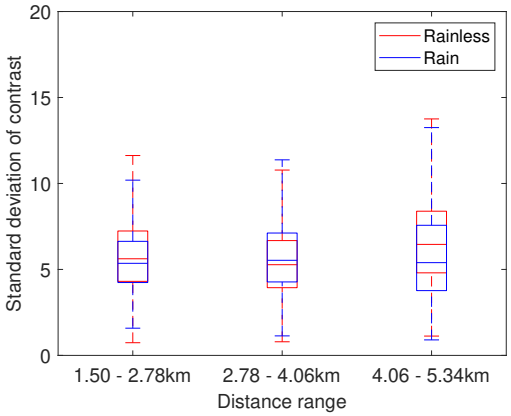

(b)

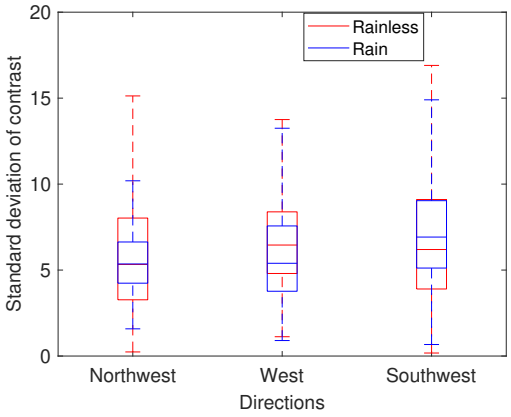

(c)

Figure 2.14: Box plots of the standard deviation distribution of contrast for different (a) wind speeds, (b) ranges, and (c) directions.

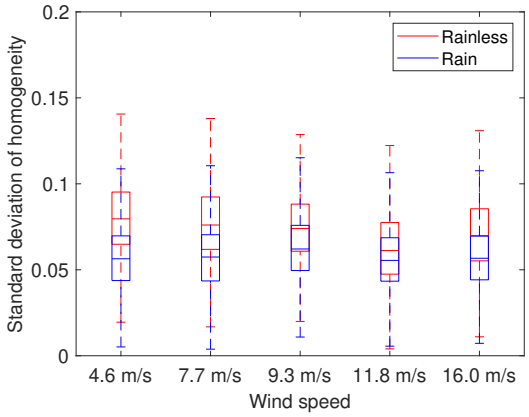

(a)

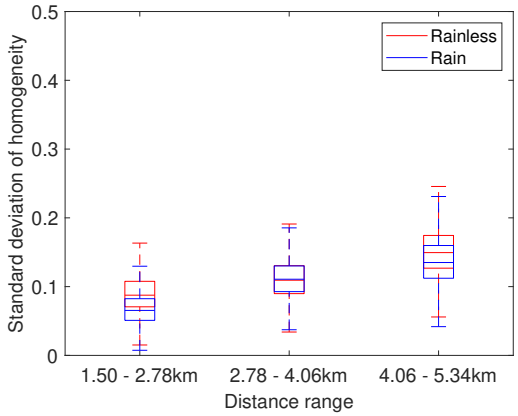

(b)

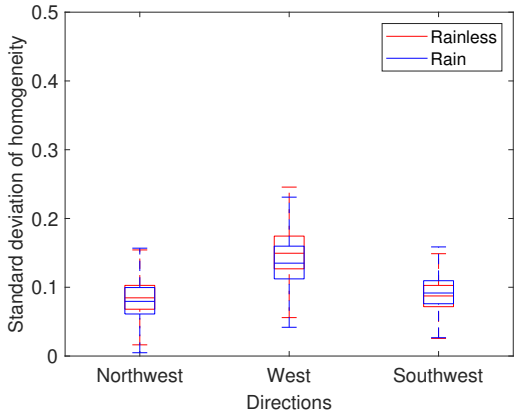

(c)

Figure 2.15: Box plots of the standard deviation distribution of homogeneity for different (a) wind speeds, (b) ranges, and (c) directions.

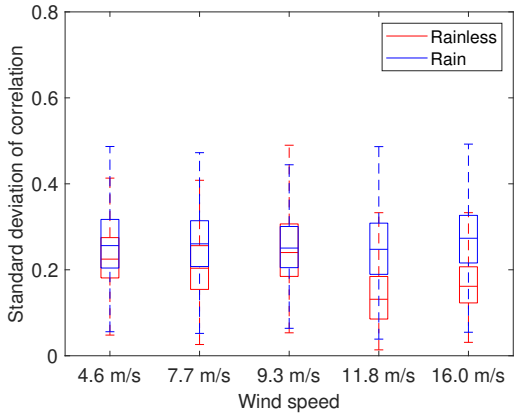

(a)

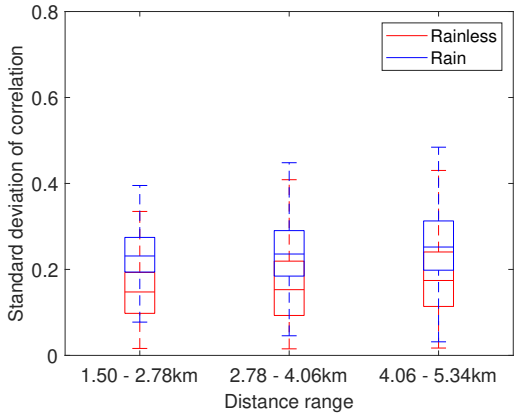

(b)

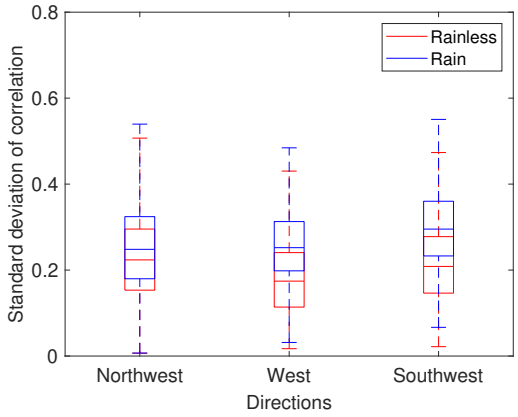

(c)

Figure 2.16: Box plots of the standard deviation distribution of correlation for different (a) wind speeds, (b) ranges, and (c) directions.

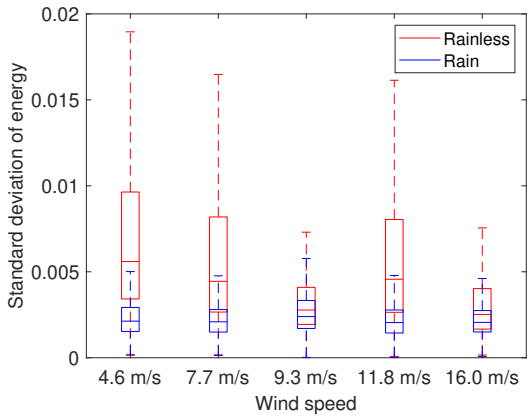

(a)

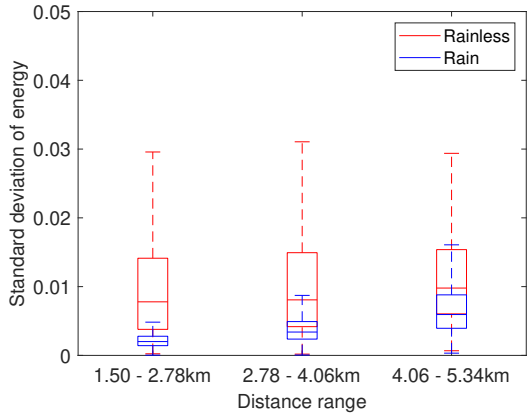

(b)

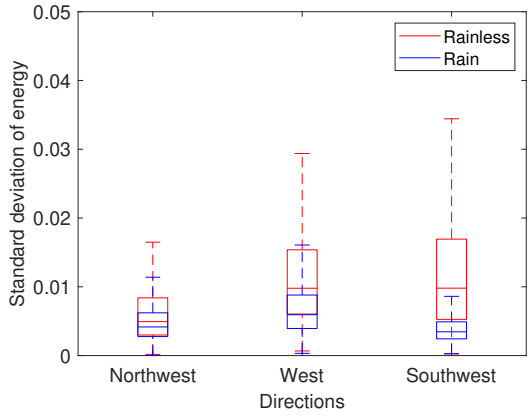

(c)

Figure 2.17: Box plots of the standard deviation distribution of energy for different (a) wind speeds, (b) ranges, and (c) directions.

under rainless conditions are larger than those obtained under rainy conditions. On the other hand, the median standard deviations calculated from the correlations under rainless conditions are smaller than that obtained under rainy conditions. Additionally, it can be found that these features do not show obvious dependence on wind speed, distance range and direction under rainless or rainy condition. According to the difference of the mean and standard deviation distributions of each feature under the rainless and rainy conditions, it can be concluded that values of these image features will mainly be influenced by rain. Thus, it is feasible to extract the mean and variance of these features as feature vectors to train the classification model.

2.3.2 Wave Direction Result Analysis

Figs. 2.18 and 2.19 show the wave direction estimation results under rainless and rainy conditions. Specifically, Figs. 2.18(a) and Fig. 2.19(a) show the simultaneous wind speed and wave height information of each sample. It can be observed from Fig. 2.18(b) that a few relatively large deviations between radar-derived results and buoy measurements appear when the sub-image selection scheme is not used under rainless conditions. These deviations are mainly caused by estimation from some low-backscatter regions in the radar images. From Fig. 2.19(c), it can be found that there are many relatively large deviations between radar-derived results and buoy measurements if the sub-image selection scheme is not applied. This is mainly caused by estimation from the regions severely contaminated by rain. In contrast, the sub-image selection scheme leads to a better performance in wave direction estimation; thus, this method can effectively mitigate the rainfall effect on estimation to some extent. As for Figs. 2.18(c) and 2.19(d), it can be found that the deviation of estimated wave direction increases with the increase of rainfall intensities. Under rainy conditions, the wave signatures may be still affected by rain even if the texture is clear in the sub-image identified by selection scheme. Another reason for the large difference between the wave direction estimated from the radar images and buoy data may be that the buoy site is far away from the coastal radar system and is not within the radar coverage range.

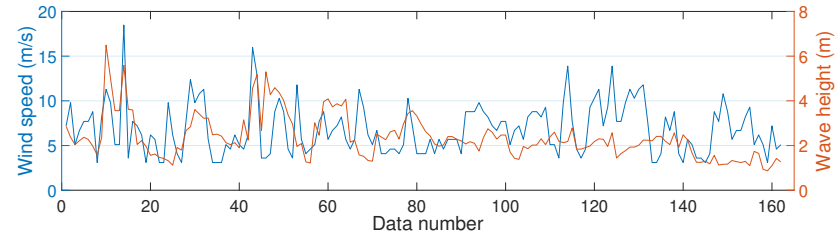

(a)

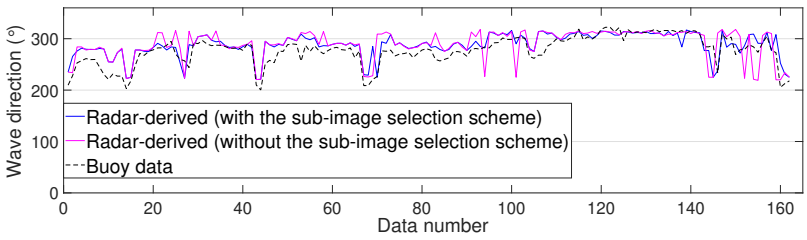

(b)

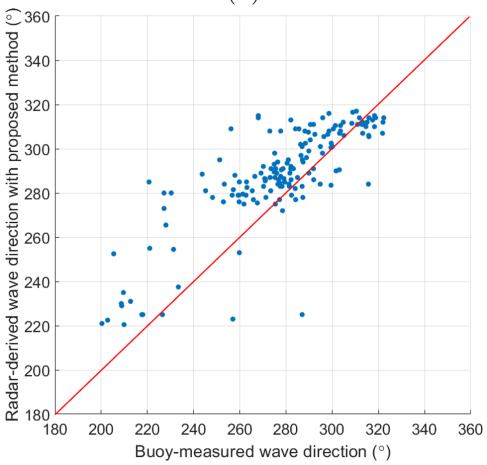

(c)

Figure 2.18: (a) Simultaneous wind speed and wave height during radar data collection periods. (b) Wave direction estimated with and without the sub-image selection scheme under rainless conditions. (c) Scatter plot of the radar-derived and buoy-measured wave direction under rainless conditions.

Moreover, there is no obvious relationship between the wave direction estimation accuracy and wind speed or wave height.

In order to further analyze, Table 2.2 shows the root-mean-square errors (RMSEs) and

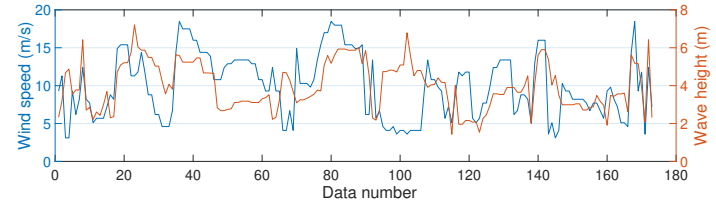

(a)

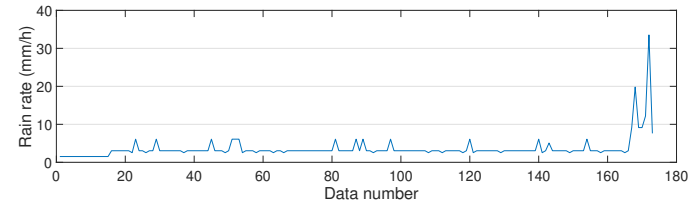

(b)

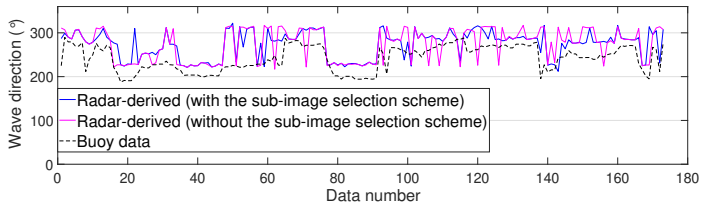

(c)

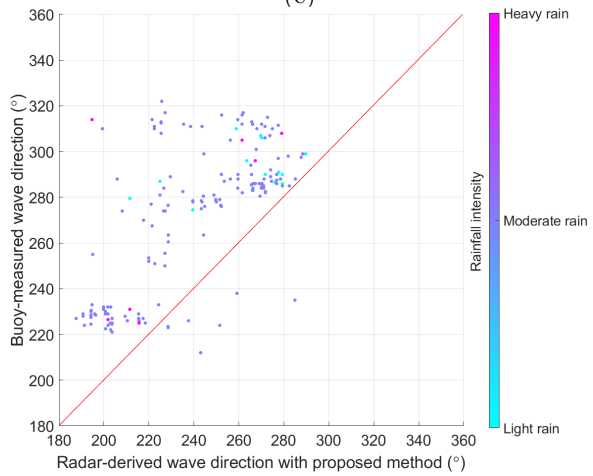

(d)

Figure 2.19: (a) Simultaneous wind speed and wave height during radar data collection periods. (b) Simultaneous rain rates during radar data collection periods. (c) Wave direction estimated with and without the sub-image selection scheme under rainfall conditions. (d) Scatter plot of the radar-derived and buoy-measured wave direction under different rainfall intensities.

Table 2.2: RMSEs and CCs of wave direction estimation under different rainfall intensities

	With sub-image selection scheme		Without sub-image selection scheme	
Rainfall intensity level	**RMSE**	**CC**	**RMSE**	**CC**
Rainless	19.7°	0.81	26.6°	0.65
Light rain	34.7°	0.44	40.7°	0.30
Moderate rain	39.8°	0.67	44.7°	0.56
Heavy rain	51.9°	0.56	52.9°	0.65

correlation coefficients (CCs) between the radar-derived and the buoy-measured wave directions. From Table 2.2, it can be observed the proposed sub-image selection scheme effectively improves estimation accuracy by reducing the RMSEs and increasing the CCs of estimation results under four rain intensity levels. Also, when rain level increases, the improvement is less. It should be noted that under heavy rain conditions, the difference between the RMSEs of wave direction is only 1°, which may be associated with the error of the buoy. However, as shown in Fig. 2.19(a)-(b), most heavy rain samples are obtained under wind speeds higher than 10 m/s. According to our previous research [22], the generated surface roughness might be dominated by wind force under high wind speeds and rain may only cause additional radar backscatter instead of blurring surface wave signatures significantly. As a consequence, wave signatures may be visible in the radar images under the heavy rain conditions. In Table 2.2, the small difference between RMSEs of wave direction under heavy rain is reasonable. In addition, the number of images obtained under heavy rain is much less than those obtained under light rain and moderate rain. Therefore, more image data obtained under the heavy rain conditions should be used to further evaluate the effectiveness of the proposed method in the future work.

2.3.3 Wave Period Result Analysis

Considering that the number of testing samples with light rain and heavy rain is small, more than one valid sub-image is extracted from light and heavy rain radar images to expand the data for wave period estimation. In [76], the optimal percentage of data used for training is found to be 40% to 80%. Thus, the whole dataset is split into 70% for training and

30% for testing in this experiment. The training set is composed of both rainless and rain-contaminated sub-images. Additionally, the proposed method with and without the sub-image selection scheme is tested. As for the method without using the sub-image selection scheme, the sub-images for wave period estimation are selected along the estimated wave direction in each radar image.

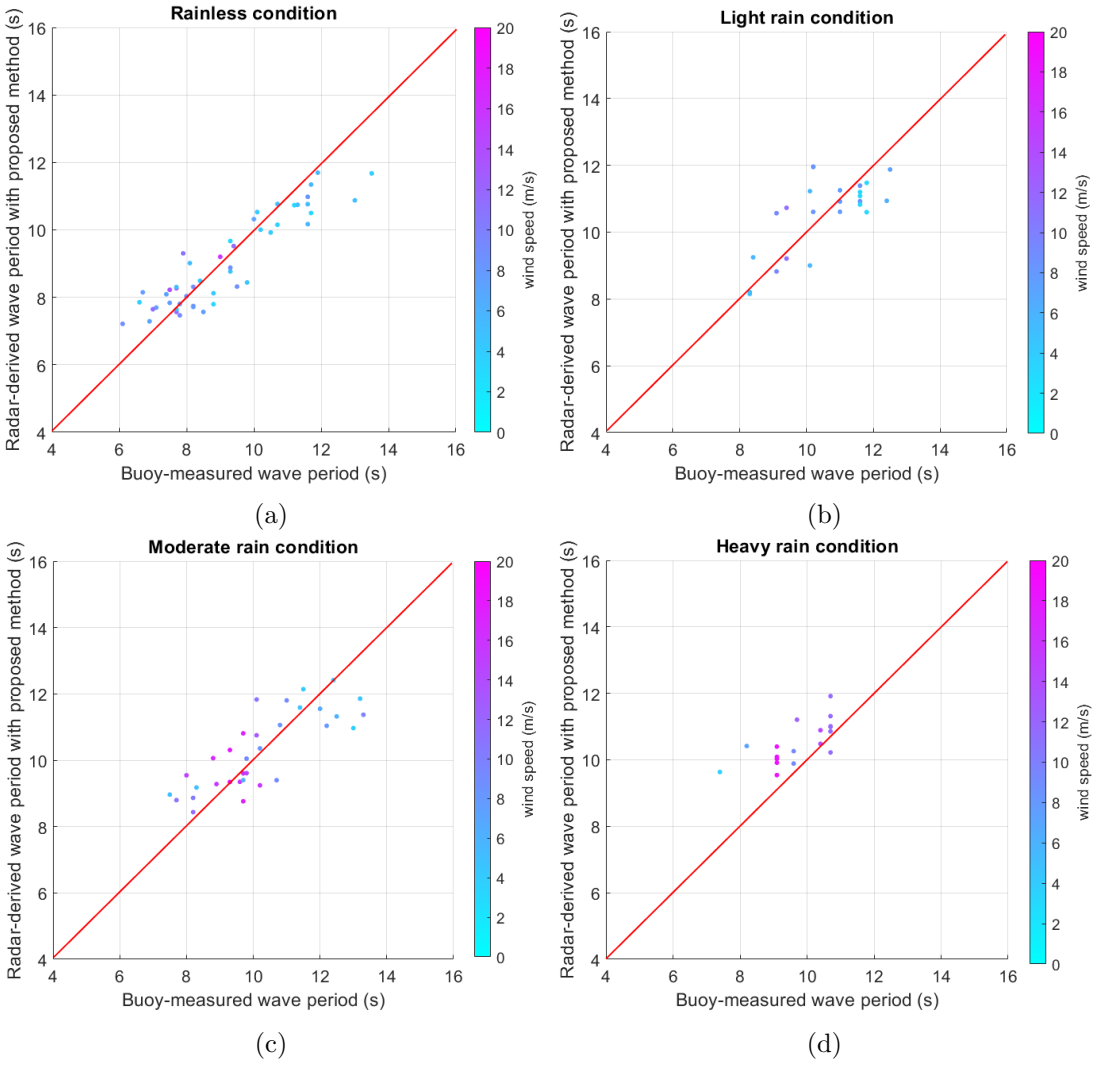

Figure 2.20: Scatter plots of radar-derived wave period with the sub-image selection scheme and buoy-measured wave period under (a) rainless conditions, (b) light rain conditions, (c) moderate rain conditions, and (d) heavy rain conditions.

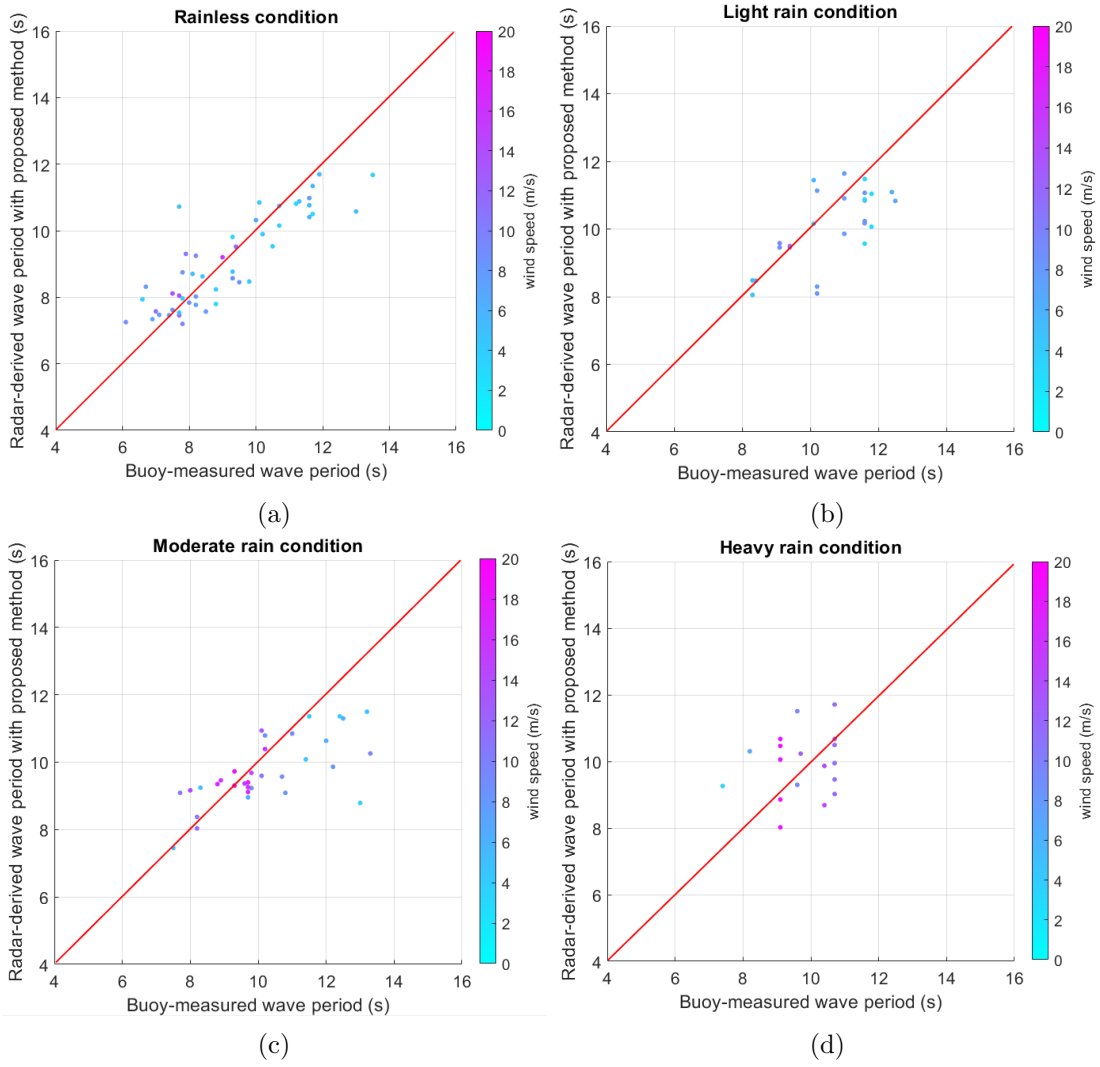

Figure 2.21: Scatter plots of radar-derived wave period without the sub-image selection scheme and buoy-measured wave period under (a) rainless conditions, (b) light rain conditions, (c) moderate rain conditions, and (d) heavy rain conditions.

Fig. 2.20 and Fig. 2.21 shows the comparison of radar-derived and buoy-measured wave periods under different rainfall intensities. Moreover, the colour intensity at each point indicates the wind speed. It can be found that the method without using the sub-image selection scheme generated larger deviations than that with the sub-image selection scheme. This is because that the wave signatures in the sub-image found by the selection scheme are less contaminated than that without using the scheme. This suggests that the sub-image

Table 2.3: RMSEs and CCs of wave period estimation under different rainfall intensities

	With sub-image selection scheme		Without sub-image selection scheme	
Rainfall intensity level	**RMSE**	**CC**	**RMSE**	**CC**
Rainless	0.80 s	0.91	0.93 s	0.86
Light rain	0.88 s	0.73	1.08 s	0.31
Moderate rain	0.98 s	0.80	1.28 s	0.69
Heavy rain	1.04 s	0.68	1.24 s	0.16

selection scheme can also efficiently mitigate the rain effect on wave period estimation. Furthermore, it also can be observed that the estimated deviation still increases with the increase of rainfall intensities. Moreover, there is no obvious relationship between the wave period estimation accuracy and wind speed.

Table 2.3 shows the RMSEs and CCs between the radar-derived and buoy-measured wave periods. It can be observed that the sub-image selection scheme helps decrease the RMSEs by 0.13 s, 0.20 s, 0.30 s under four rainfall intensity levels, respectively. On the other hand, the CCs of estimated wave periods using the sub-image selection scheme are also higher than the results without using the sub-image selection scheme under the same rainfall intensity. It can be found that the RMSE of the wave period under moderate rain condition is the largest when the sub-image selection scheme is not used. As mentioned earlier, wave signatures may still be visible in the radar images under heavy rain conditions. In contrast, those moderate rain samples obtained under low wind speeds will be dominated by rain echoes with few visible wave signatures; hence, the estimation accuracy of those samples will decrease and the corresponding RMSE is relatively large.

2.4 Chapter Summary

In this chapter, the influence of rainfall intensity on wave direction and period estimation from X-band marine radar images is analyzed. First, a random-forest-based classification method for identifying the valid sub-images with visible wave signatures is proposed to reduce the effect of rain. Wave direction is estimated from the selected valid sub-images

of each radar image by performing a RT-based algorithm, while a novel method based on texture feature extraction, and a random-forest-based regression model is proposed for wave period estimation. Experimental results show that the sub-image selection scheme plays a significant role in reducing wave direction and wave period estimation errors under different rain conditions. In addition, it has been observed that as rain rate increases, the influence of rain on wave parameter estimation tends to be more severe as well. As a limitation of this method, the time required for GLCM feature extraction from a radar image is around 54 s. Therefore, a more efficient method for GLCM feature extraction should be developed.

Chapter 3

Wave Height Estimation from X-band Nautical Radar Images Using Temporal Convolutional Network

In this chapter, a temporal convolutional network (TCN)-based significant wave height (H_s) estimation model that employs three types of H_s-related input features is proposed. In Section 3.1, the radar and wave data used in this study are introduced. The procedures for feature extraction and the architecture of TCN are described in Section 3.2. Section 3.3 illustrates the experimental results and comparisons among different ML-based algorithms. Finally, conclusions and future work are addressed in Section 3.4.

3.1 Data Overview

In this chapter, since H_s estimation is studied under rainless condition, another set of data with more available rain-free radar images is utilized for analysis. Additionally, the data

used in Chapter 2 do not provide radar image sequences and thus do not permit utilization of temporal features to analyze H_s. The radar data in this chapter were collected by an X-band nautical radar (Decca) operating at grazing incidence with horizontal transmit and horizontal receive (HH) polarization. The radar system was installed on a moving vessel and its information is provided in Table 3.1. During the data collection periods (from November 26 to December 4, 2008), the vessel was travelling approximately 300 km south-southeast of Halifax, Nova Scotia, Canada, where the water depth is around 200 m. Since the antenna rotation period is around 2.14 s, each sequence file which includes 32 radar gray-level (from 0 to 255) images is generated approximately every 68 seconds by WaMoS II. The original radar images are presented in polar coordinates and can be transformed into Cartesian coordinate through scan conversion. It should be noted that because the presence of rain may blur wave signatures and lead to inaccurate wave estimation [21, 57], data collected under rainfall conditions are excluded from the analysis. Simultaneous wave measurements from three Triaxys directional wave buoys that were deployed in a drifting mode [77] are used as ground truth for model training, validation, and testing purposes. In order to maintain a short distance from the drifting buoys, the vessel was sailed or moored near the buoys during the data collection period. The distances between the vessel and the buoys were generally less than 10 km. The route of the vessel is indicated by red lines in Fig.3.1. Those buoys are able to measure H_s ranging from 0 to 20 m with a resolution of 0.01 m, and an error within 2%. Since the reference H_s was measured approximately every 30 minutes, the simultaneous H_s for each radar image sequence can be obtained by temporal averaging and interpolation.

3.2 Methodology

3.2.1 Feature Extraction

In this study, three types of features are extracted using different algorithms and combined as the input feature vector for the estimation model. These features are introduced below.

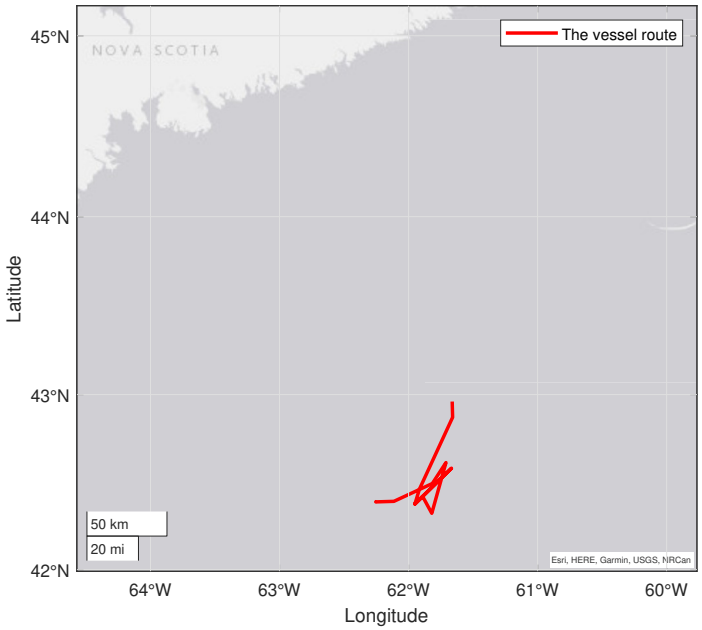

Figure 3.1: The route of the vessel during radar data collection periods.

SNR feature extraction

In [18], SNR was calculated from radar-derived wave spectra based on 3D Fourier transform analysis and it used to determine H_s through linear regression. Here, a series of 32 Cartesian radar images contained in each file are used to generate one estimation result. For each radar image, a 128 × 128 sub-image (960 m × 960 m) centered on the upwind direction was selected, as shown in Fig. 3.2. The calculation of SNR involves several steps. Firstly,

Table 3.1: Radar information

Transmit frequency	9.41 GHz
Polarization	Horizontal
Pulse width	50 ns
Range resolution	7.5 m
Range coverage	240 m - 2160 m
Beam width	2°
Azimuth coverage	360°
Antenna height	21.9 m
Antenna rotation speed	28 rpm
Grey level of radar image	0 - 255

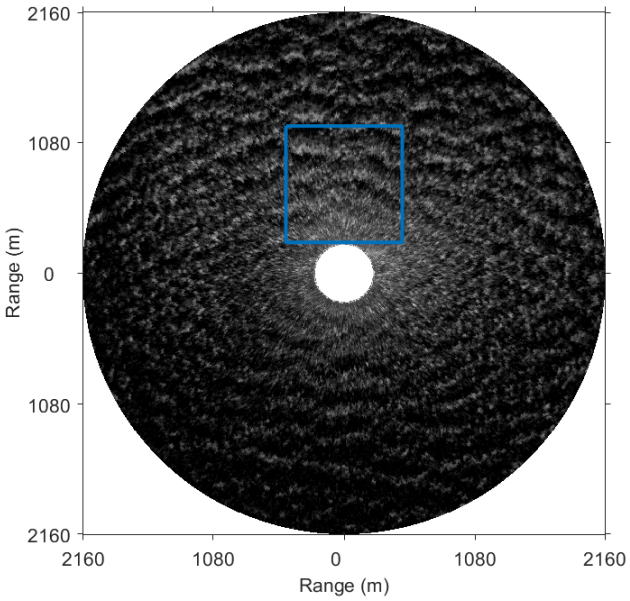

Figure 3.2: The selected sub-image (outlined in blue) for calculating SNR.

the image spectrum of the selected region $F_I(\boldsymbol{k}, \omega)$ is obtained by applying the 3D Fourier transform [8], where $\boldsymbol{k} = (k_x, k_y)$ is the two-dimensional wave number vector and ω is the angular frequency of the ocean wave. According to the linear gravity wave theory [8, 33], the dispersion relation can be expressed as

$$\omega = \sqrt{g|\boldsymbol{k}| \tanh{(|\boldsymbol{k}|d)}} + \boldsymbol{k} \cdot \boldsymbol{U}, \tag{3.1}$$

where d is the water depth, g is the gravitational acceleration, and $\boldsymbol{U} = (U_x, U_y)$ is the velocity of encounter (i.e., combination of the velocities of radar platform and current) [33, 78]. Then, $\boldsymbol{U}$ can be determined by a least square analysis method using the dispersion relation (3.1) according to the image spectrum [8, 19]. The high harmonic dispersion relation is also considered and may be expressed as

$$\omega_q = (q+1)\sqrt{\frac{g|\boldsymbol{k}|}{q+1} \tanh{(\frac{|\boldsymbol{k}|d}{q+1})}} + \boldsymbol{k} \cdot \boldsymbol{U}, \tag{3.2}$$

where q represents the order of the q^{th}-harmonic. The main spectral components of the image spectrum include the wave-related component, high harmonics caused by shadowing modulation, subharmonics of the dispersion relation, and the background spectral noise (BGN) due to the roughness caused by the local wind on the sea surface [79]. The wave-related image spectrum (denoted as $F_F(\boldsymbol{k},\omega)$) can be extracted from $F_I(\boldsymbol{k},\omega)$ by applying a filter based on the linear wave dispersion relationship (3.1). Hence, those components in the image spectrum that do not belong to the wave field can be filtered [8]. Similarly, the high harmonic spectrum (denoted as $F_H(\boldsymbol{k},\omega)$) also can be obtained from $F_I(\boldsymbol{k},\omega)$ (3.2).

Thus, the 3D BGN spectrum (denoted as $F_{BGN}(\boldsymbol{k},\omega)$) can be approximated as

$$F_{BGN}(\boldsymbol{k},\omega) \simeq F_I(\boldsymbol{k},\omega) - F_F(\boldsymbol{k},\omega) - F_H(\boldsymbol{k},\omega). \tag{3.3}$$

Next, due to the non-linearity of the radar imaging process, the wave spectrum (denoted as $F_W(\boldsymbol{k},\omega)$) is estimated from $F_F(\boldsymbol{k},\omega)$ using an empirical modulation transfer function (MTF, denoted as $T_M(\boldsymbol{k})$) as

$$F_W(\boldsymbol{k},\omega) = F_F(\boldsymbol{k},\omega) \cdot T_M(\boldsymbol{k}). \tag{3.4}$$

The MTF ($T_M(\boldsymbol{k})$) is used for converting the wave-related image spectrum to the actual wave spectrum as a further correction, which is expressed as

$$T_M(\boldsymbol{k}) = |\boldsymbol{k}|^{\beta}, \tag{3.5}$$

where β is the MTF exponent, which is empirically suggested as 1.2 [11]. Finally, the SNR can be obtained as the ratio of the integration of the wave spectrum and the integration of BGN as

$$\mathrm{SNR} = \frac{\int_{\Omega_{\boldsymbol{k}}^{\alpha}} \mathrm{F_W}(\boldsymbol{k},\omega)\mathrm{d}^2\mathrm{k}\mathrm{d}\omega}{\int_{\Omega_{\boldsymbol{k}}^{\omega}} \mathrm{F_{BGN}}(\boldsymbol{k},\omega)\mathrm{d}^2\mathrm{k}\mathrm{d}\omega}. \tag{3.6}$$

Finally, the calculated $\sqrt{\mathrm{SNR}}$ is considered as the SNR feature for the network model since it has been found that $\sqrt{\mathrm{SNR}}$ is proportional to H_s [18].

EEMD feature extraction

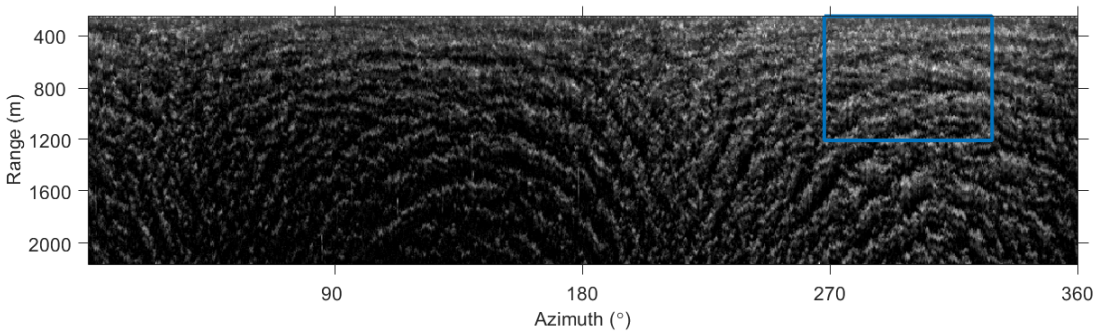

Figure 3.3: The selected sub-image (outlined in blue) for EEMD-based feature extraction.

In order to reduce the computation load, a sub-image ranging from 240 to 1200 m from the radar site and ±30° around the upwind direction was selected for feature extraction from the first polar radar image in each sequence file, as displayed in Fig. 3.3. The details of feature extraction are illustrated as follows. Firstly, the sub-image can be represented by I_{sub} as

$$I_{sub} = \begin{bmatrix} p_{(1,1)} & p_{(1,2)} & \cdots & p_{(1,N)} \\ p_{(2,1)} & p_{(2,2)} & \cdots & p_{(1,N)} \\ \vdots & \vdots & \ddots & \vdots \\ p_{(M,1)} & p_{(M,2)} & \cdots & p_{(M,N)} \end{bmatrix}, \tag{3.7}$$

where $p_{(m,n)}$ is the intensity of the pixel in the m^{th} row and the n^{th} column of the sub-image. Then, ensemble empirical mode decomposition (EEMD) [36] is applied to each column (azimuthal direction) of I_{sub} to obtain the first five intrinsic mode functions (IMFs) and a residual term, which can be obtained as

$$I_{sub}(\sim, n) = \sum_{j=1}^{5} C_j(\sim, n) + R(\sim, n), \tag{3.8}$$

where n is the n^{th} column of the sub-image, C_j is the j^{th} IMF, and R is the residual term. Each IMF can be split into the amplitude modulation (AM, denoted as A) and frequency modulation (FM, denoted as F) portions [80] using a normalization scheme, where the AM

part $A_j(\sim, n)$ is expressed as

$$A_j(\sim, n) = \begin{bmatrix} a_{1,n,j} \\ a_{2,n,j} \\ \vdots \\ a_{M,n,j} \end{bmatrix}. \tag{3.9}$$

Eventually, the AM portions of the 2^{nd}-5^{th} IMFs are calculated and averaged in each azimuth and range of the sub-image, which can be expressed as

$$S = \frac{1}{N}\frac{1}{M}\sum_{j=2}^{5} A_j. \tag{3.10}$$

In [36], the calculated average (S) is used to estimate H_s with linear regression. Here, it is employed as another input to the network model.

GLCM feature extraction

Since GLCM analysis has already been employed for retrieving wave direction and wave period [81], it is reasonable to further analyze GLCM-based features for H_s estimation. The selected region for feature extraction is the same as the region extracted for the EEMD feature. A 29×29 sliding window (217.5 m $\times$ 217.5 m) is first applied to the sub-image. The distance between the pixel pairs in each sliding window is set as 4, while the positional relationships of pixel pairs are in four directions (0°, 45°, 90°, and 135°) [66]. In this study, four statistics calculated from each GLCM, i.e., contrast (Con), homogeneity (H), correlation (Cor), and energy (E) are selected. In order to verify the influence of different H_s on the GLCM feature values, the median values of mean and standard deviation of the four features over four directions from all sliding windows in each radar sub-image are calculated and compared under different H_s ranges (1.00 - 2.25 m, 2.25 - 3.50 m, 3.50 - 4.75 m), as shown in the box plots in Figs. 3.4 and 3.5. It can be observed that only two (i.e., the median values of mean contrast and mean homogeneity) out of the eight figures do not show clear correlations with H_s, while the other six features either increase or decrease gradually

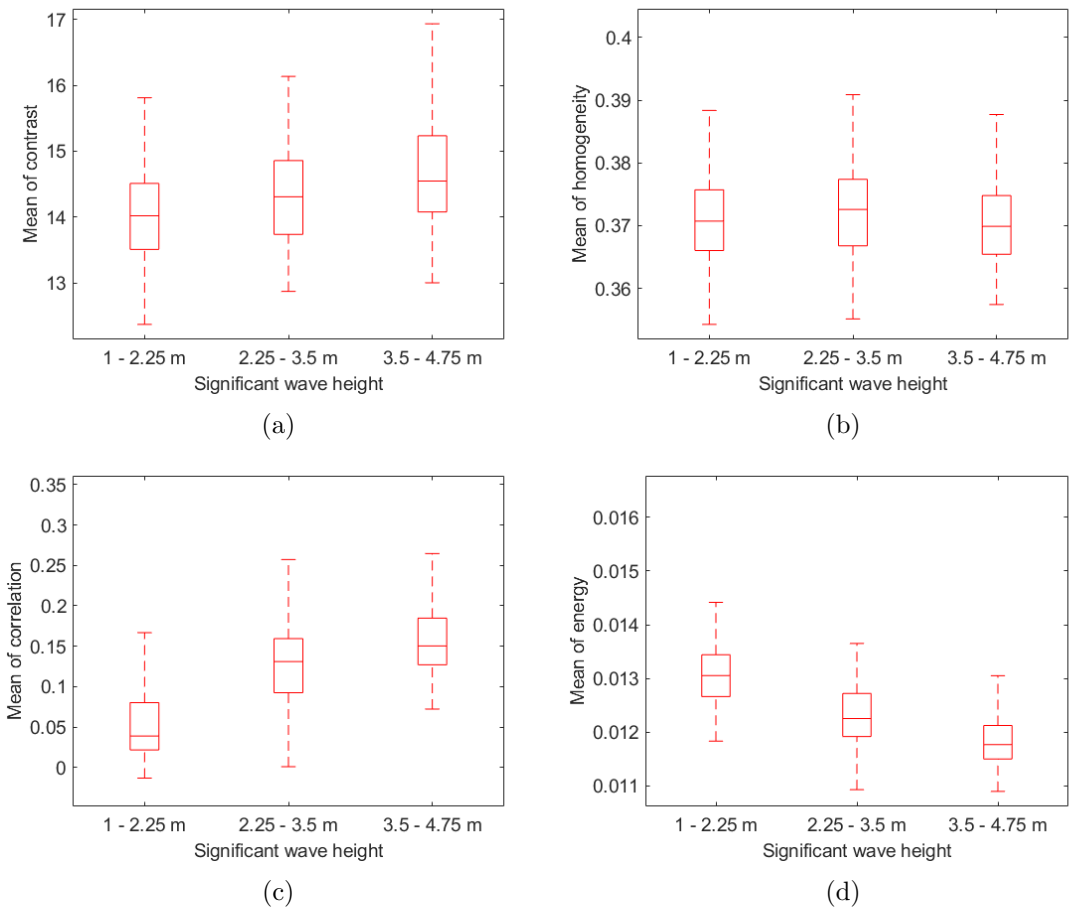

Figure 3.4: Median value distribution of mean of (a) contrast, (b) homogeneity, (c) correlation, and (d) energy.

as H_s increases. Thus, metrics presented in the other six figures are selected from each radar image for H_s estimation, i.e.,

- Median of mean correlation;
- Median of mean energy;
- Median of contrast standard deviation;
- Median of homogeneity standard deviation;
- Median of correlation standard deviation;
- Median of energy standard deviation.

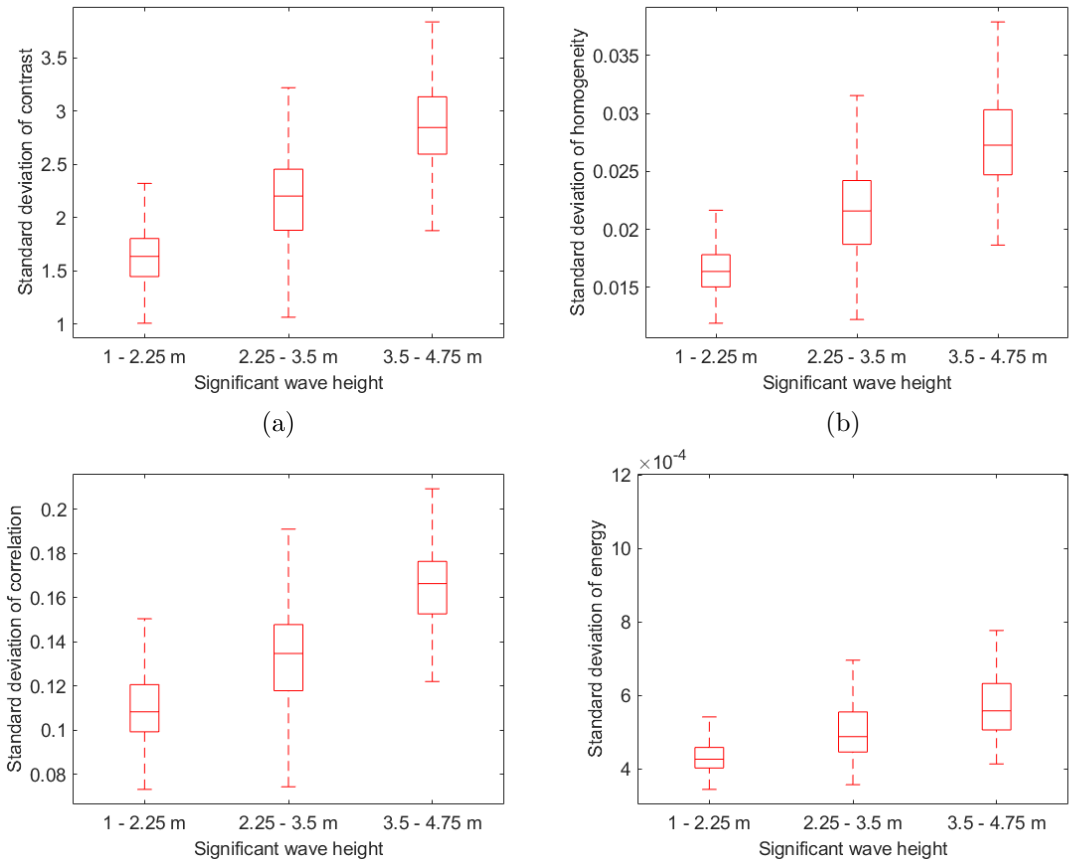

Figure 3.5: Median value distribution of standard deviation of the (a) contrast, (b) homogeneity, (c) correlation, and (d) energy.

Those 6 features are combined with the SNR and EEMD features to form a feature vector. Then, the combined feature vector is normalized by using zero-center normalization. Assume that the collection of each type of feature extracted from all sequences is denoted as T, the normalization operation results in

$$T_{norm} = \frac{T - \text{mean}(T)}{\text{std}(T)}, \tag{3.11}$$

where T_{norm} is the collection of each type of normalized feature, and mean(T) and std(T) are the mean value and standard deviation, respectively, of each type of feature collection in all sequences. Finally, a total of 8 normalized features are combined as an 8-dimensional

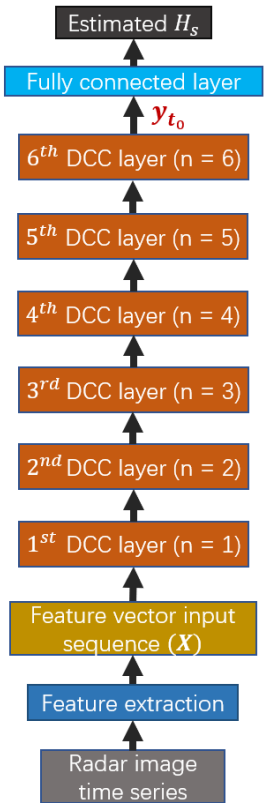

Figure 3.6: The overall framework of the TCN-based H_s estimation model.

(8D) feature vector for each input sample in the TCN-based model.

3.2.2 TCN-based Wave Height Estimation Model

TCN is a variant of CNN that convolves over the time domain. The complete architecture of the proposed TCN-based H_s estimation model is presented in Fig. 3.6, which includes 6 dilated causal convolution (DCC) layers and a fully connected layer. The functions of each component and operation in the network are briefly introduced as follows.

DCC layer

The visualization of dilated convolution inside 6 DCC layers is shown in Fig. 3.7. It can be observed that the outputs of each convolutional layer are calculated only from its current and

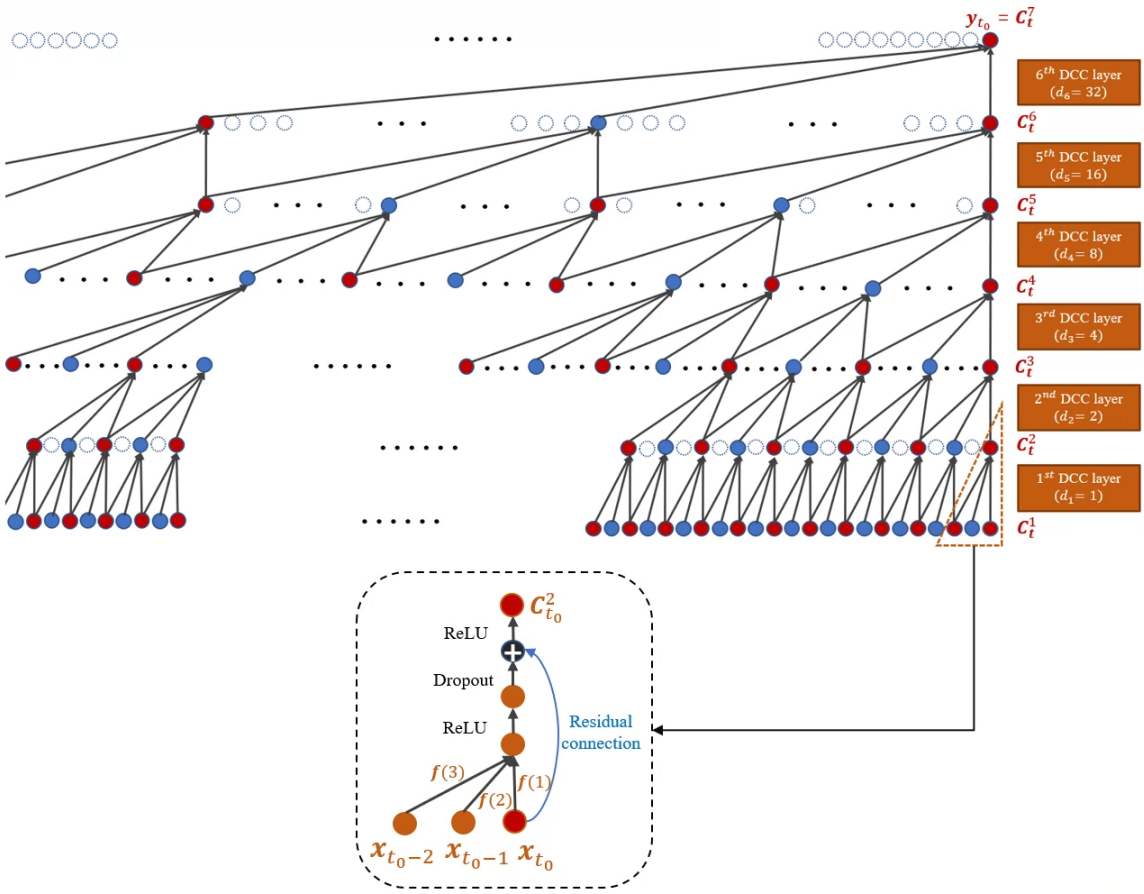

Figure 3.7: Visualization of dilated convolution in 6 DCC layers.

earlier input samples. On the other hand, it also allows interval sampling of the input during convolution, which allows a larger number of effective history inputs without a pooling [82]. As shown in Fig. 3.7, the sampling rate is controlled by the dilation factor, which increases exponentially with the depth of the network. For the n^{th} DCC layer, the dilation factor is given by $d_n = 2^{(n-1)}, n \in \{1, 2, ..., 6\}$. Also, the filter size in each convolution operation is $k \times 1$. In this study, k is equal to 3 since if the value of k is too large or too small, the computation load will be increased or the temporal feature cannot be reflected, respectively. The number (r) of input samples in the receptive field of this network is determined by d_n and k, resulting in

$$r = 1 + \sum_{n=1}^{6} (k-1) \times d_n = 127. \tag{3.12}$$

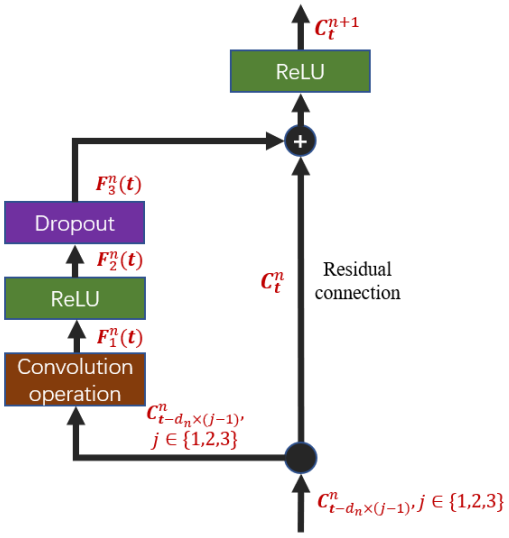

Figure 3.8: The structure of each DCC layer.

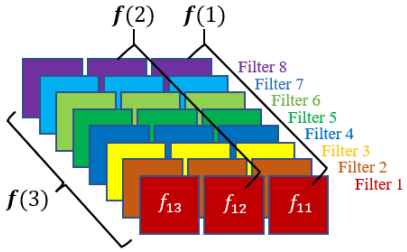

Figure 3.9: A figure illustration of 8 3×1 filters used in the convolution operation.

As mentioned above, each sample in the input sequences ($\boldsymbol{X}$) consists of an 8D feature vector. In order to estimate H_s at a certain time (t_0) in the sequences, a total of 127 8D feature vectors ($\boldsymbol{x}_{t_0}, \boldsymbol{x}_{t_0-1}, ..., \boldsymbol{x}_{t_0-126}$) are extracted as the receptive field to produce an 8D result ($\boldsymbol{y}_{t_0}$) from 6 DCC layers.

The detailed calculation steps in each DCC layer are illustrated in Fig. 3.8, which includes a convolution operation, rectified linear unit (ReLU), and dropout. A total of 8 filters are used in each convolution operation. In particular, all elements in 8 filters can be denoted as $f_{ij}, i \in \{1,2,3,4,5,6,7,8\}, j \in \{1,2,3\}$, where i represents the index of

filters and j represents the index of elements in the i^{th} filter. The values of each filter are initialized with a normal distribution. As displayed in Fig. 3.9, the collections of f_{i1}, f_{i2}, and $f_{i3}, i \in \{1,2,3,4,5,6,7,8\}$ are respectively denoted as three 8D vectors $\boldsymbol{f}(1)$, $\boldsymbol{f}(2)$, and $\boldsymbol{f}(3)$ for the convolution operation. In Fig. 3.7, $\boldsymbol{C}_{\boldsymbol{t}}^{n}$ indicates the input of convolution operation at time $\boldsymbol{t}$ in the n^{th} DCC layer, which is marked in red. Due to the dilation, $\boldsymbol{t}$ of each input sample used in the n^{th} DCC layer can be expressed as

$$\boldsymbol{t} = t_0 - 2^n \times l, l \in \{0, 1, ..., 2^{7-n} - 2\}. \tag{3.13}$$

Therefore, the output of the convolution operation at time $\boldsymbol{t}$ in the n^{th} DCC layer can be expressed as

$$\boldsymbol{F}_1^n(\boldsymbol{t}) = \sum_{j=1}^{3} \boldsymbol{f}(j) * \boldsymbol{C}^n_{\boldsymbol{t}-d_n\times(j-1)}, \tag{3.14}$$

where $*$ denotes the element-wise product. When $n = 1$, the inputs can be given as $\boldsymbol{C}^1_{\boldsymbol{t}-d_1\times(j-1)} = \boldsymbol{x}_{\boldsymbol{t}-d_1\times(j-1)}$.

Then, the convolution operation is followed by ReLU. ReLU is a kind of activation function [83] that sets all negative input values to zero in order to achieve non-linear transformation of the data, which is given by

$$\boldsymbol{F}_2^n(\boldsymbol{t}) = \mathrm{ReLU}(\boldsymbol{F}_1^n(\boldsymbol{t})). \tag{3.15}$$

Compared to other activation functions, ReLU further reduces computation by adding more sparsity.

In order to prevent overfitting, the dropout operation is used as a form of regularization after ReLU [84], which will probabilistically drop out nodes in the network during the training. Assuming that output values in the ReLU operation are kept for futher computation with a probability of p, the expression can be presented as

$$\boldsymbol{F}_3^n(\boldsymbol{t}) = \boldsymbol{M} * \boldsymbol{F}_2^n(\boldsymbol{t}), \tag{3.16}$$

where $\boldsymbol{M}$ is the 8D vector consisting of 0 and 1, which is generated by the Bernoulli function

$$\boldsymbol{M} \sim \text{Bernoulli}(p). \tag{3.17}$$

In the proposed model, the probability p is set as 50% in each dropout operation, which means half of the randomly selected output values will be kept while the other half are discarded.

Furthermore, the residual connection [85] is incorporated into the training of deep layers in order to avoid the issue of exploding or vanishing gradients. Specifically, the input of each convolution operation at time $\boldsymbol{t}$ is connected to the output from the dropout operation for the addition operation [63]. Then, after the addition operation, the ReLU operation is implemented. The output ($\boldsymbol{C}_{\boldsymbol{t}}^{n+1}$) can be expressed as

$$\boldsymbol{C}_{\boldsymbol{t}}^{n+1} = \text{ReLU}(\boldsymbol{F}_3^n(\boldsymbol{t}) + \boldsymbol{C}_{\boldsymbol{t}}^n). \tag{3.18}$$

When $n \leq 5$, $\boldsymbol{C}_{\boldsymbol{t}}^{n+1}$ is considered as the input at time $\boldsymbol{t}$ of next layer. When $n = 6$, $\boldsymbol{t}$ is equal to t_0. Thus, $\boldsymbol{C}_{\boldsymbol{t}}^{6+1}$ can also be written as $\boldsymbol{y}_{t_0}$.

Fully connected layer

The purpose of this step is to establish the mapping relationship between the 8D output ($\boldsymbol{y}_{t_0}$) from 6 DCC layers and the final estimated wave height (H_{est}). Assume that $\boldsymbol{y}_{t_0} = (y_1, y_2, ..., y_8)$, H_{est} can be obtained as

$$H_{est} = \sum_{i=1}^{8} (w_i y_i + b_i), \tag{3.19}$$

where w_i and b_i are the updated weight value and bias corresponding to y_i by the Adam algorithm [86].

Table 3.2: RMSE comparison of estimated H_s for different input features

Input features	RMSEs of estimated H_s using TCN		
	Training	Validation	Testing
SNR	0.67 m	0.57 m	0.58 m
EEMD	0.42 m	0.41 m	0.41 m
GLCM	0.34 m	0.39 m	0.41 m
SNR +EEMD	0.42 m	0.38 m	0.39 m
SNR +GLCM	0.30 m	0.37 m	0.38 m
EEMD+GLCM	0.29 m	0.36 m	0.35 m
SNR + EEMD+GLCM	0.26 m	0.32 m	0.32 m

3.3 Experimental Results

3.3.1 Model Training

Since data collections were interrupted due to system failure for some periods, and the radar data collected under rain condition are also excluded, a total of 1448 radar image sequences were utilized in this study. 50% of radar image sequences collected in three time periods are used for model training, while the other half are used for testing the estimation accuracy. Five fold cross validation is applied to the training set. As for the model training, the size of mini-batch is referred to the widely used size (64) for a neural network. In addition, the number of epochs is set to be 150. If the number is too large, it will cost much time. On the other hand, less epochs may cause underfitting.

3.3.2 Input Features Validity Analysis

Table 3.2 shows the RMSEs of H_s estimated from the testing samples. In order to validate the effectiveness of the extracted features (SNR, EEMD, and GLCM feature) in wave height estimation, different feature combinations are input to the TCN model for the H_s estimation analysis. In this study, the range of H_s encountered is from 1.41 m to 4.49 m. It can be noticed that the regression accuracy is not satisfactory when only the SNR feature is used as the input feature for the network, while the regression result is better when EEMD or GLCM is selected as the single input. When selecting two of the three features, it is noticed

that combination with the GLCM feature generate better results than combinations without the GLCM feature. It can be observed that when the SNR feature is added to the combined features of EEMD and GLCM, the performance of H_s estimation can be further improved to produce the minimum RMSE.

3.3.3 Comparisons with Different Methods

In order to compare the performance of the TCN-based model with existing methods for estimating H_s from the radar data, the typical SNR-based [18] and EEMD-based [36] linear fitting methods are also implemented. The SVR-based [87] and CGRU-based models [88] with the same input features as the TCN model are also employed for comparison. The estimation results from the testing samples with the SNR-based linear fitting, EEMD-based linear fitting, SVR-based, CGRU-based and the proposed TCN-based methods before and after implementing the moving average are presented in Figs. 3.10(a), (b), (c), (d), and (e), respectively. The temporal moving average is applied to the estimated H_s obtained during each time interval between two consecutive buoy measurements. In addition, Fig. 3.11 shows the estimated H_s of all samples before and after applying the moving average in time series. It can be noticed from Fig. 3.10(a) and Fig. 3.11(a) that the SNR-based linear fitting method does not present a clearly linear relationship between the square root of SNR and H_s. Specifically, H_s is generally overestimated when the buoy-measured H_s is lower than 3 m and mostly underestimated for higher H_s. In the SNR-based linear fitting method, wave height is assumed to be linearly related with $\sqrt{\text{SNR}}$. However, this may not be true for all H_s values. Fig. 3.10(b) and Fig. 3.11(b) show that for EEMD-based method, H_s will be overestimated for buoy-measured H_s lower than 3.5 m. In contrast, the proposed TCN-based method is able to estimate H_s without significant bias.

The RMSEs, correlation coefficients (CCs), and biases between the radar-derived H_s of the various methods, as well as the buoy-measured H_s, are summarized in Table 3.3. It can be observed that the RMSE calculated from the TCN model is 0.32 m and the CC

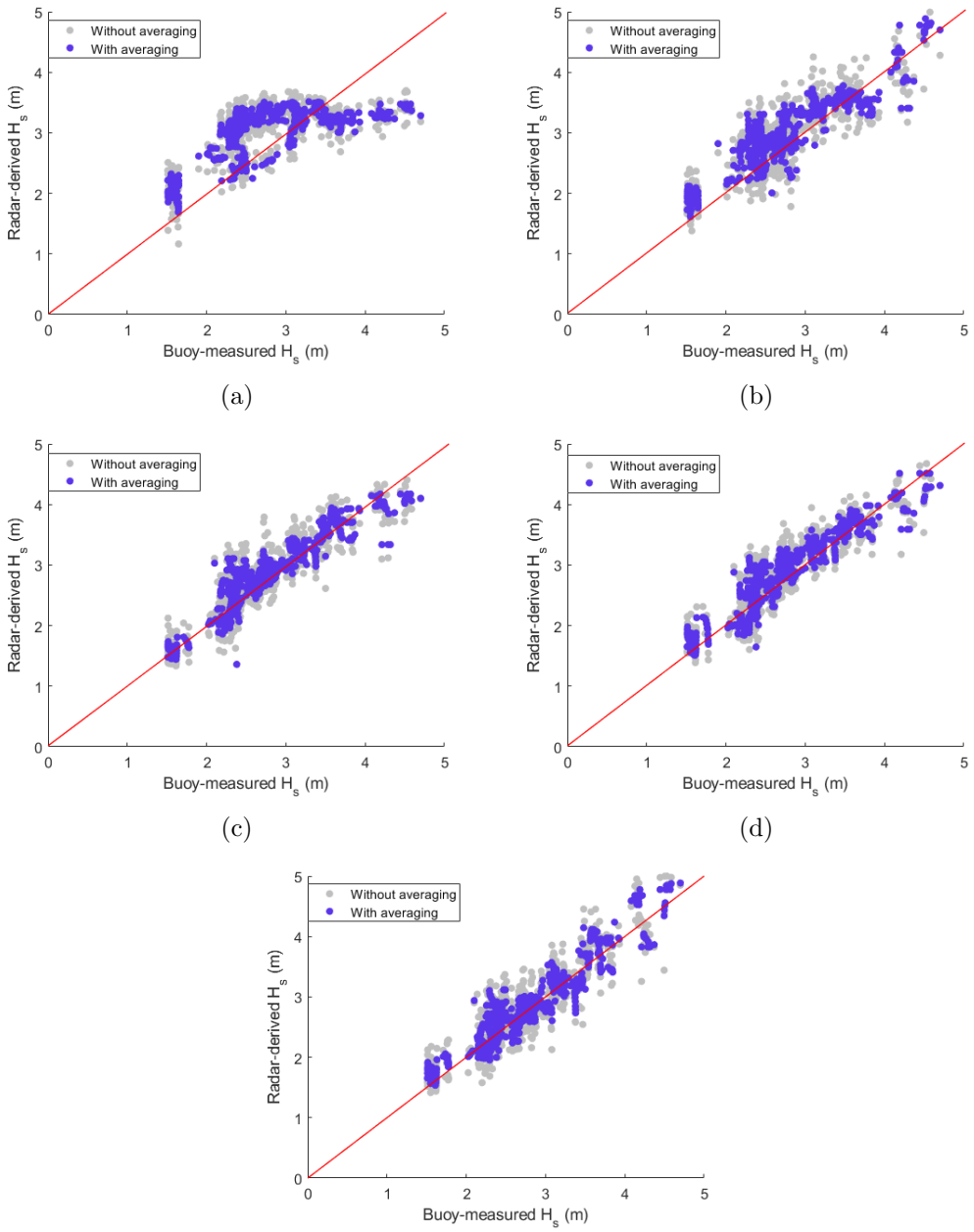

Figure 3.10: Scatter plots of buoy-measured H_s and radar-derived H_s with and without temporal moving average. (a), (b), (c), (d), and (e) correspond to SNR-based linear fitting, EEMD-based linear fitting, SVR-based and GRU-based, and the proposed TCN-based methods, respectively.

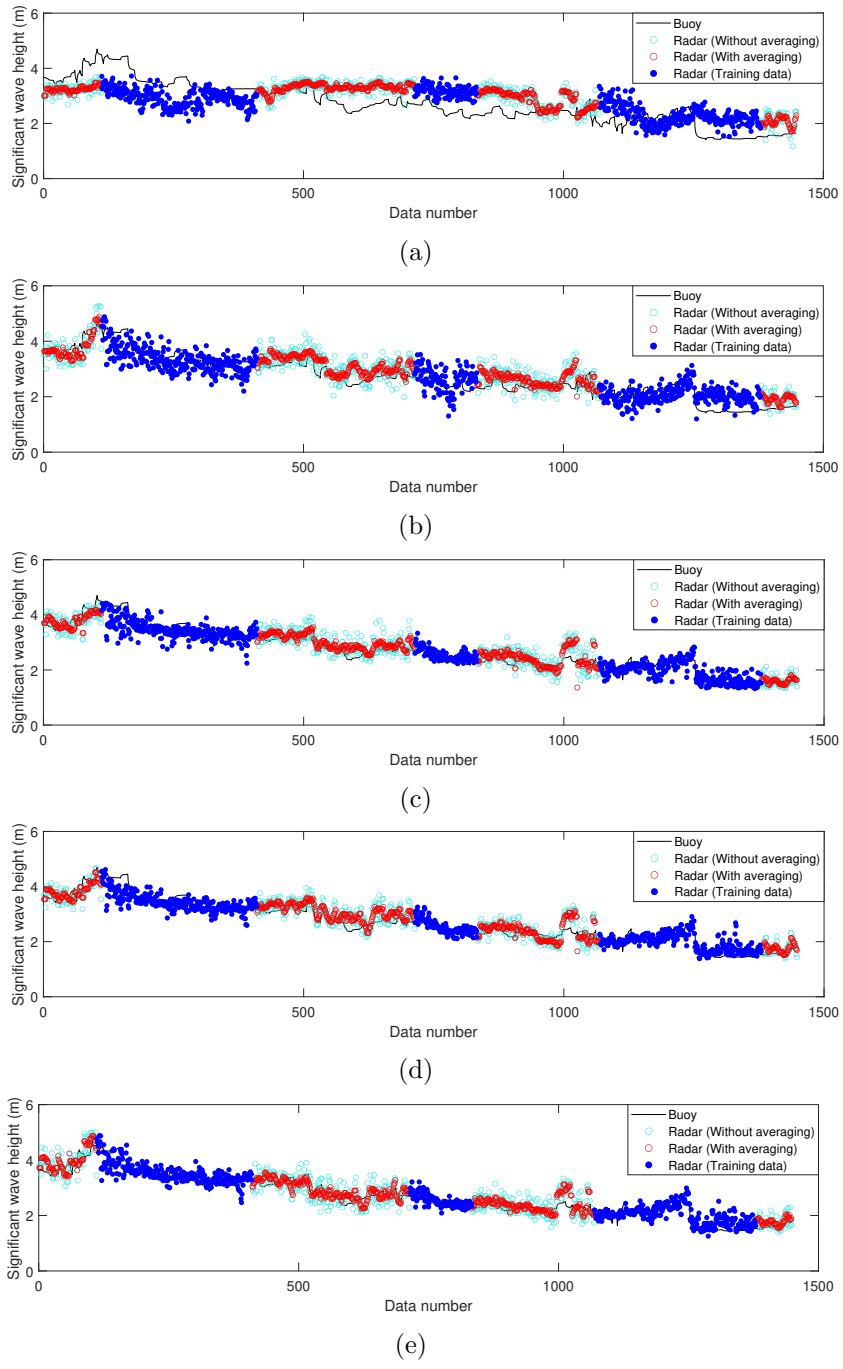

Figure 3.11: H_s estimation results in time series using different methods. Cyan and red scatters represent testing samples without and with temporal averaging, respectively. (a), (b), (c), (d), and (e) correspond to SNR-based linear fitting, EEMD-based linear fitting, SVR-based and GRU-based, and the proposed TCN-based methods, respectively.

Table 3.3: Comparisons of results using different methods for H_s estimation

	Training			Validation			Testing (without averaging)			Testing (with averaging)		
	RMSE	CC	Bias	RMSE	CC	Bias	RMSE	CC	Bias	RMSE	CC	Bias
SNR-based linear fitting method	0.68 m	0.59	-0.01 m	–	–	–	0.59 m	0.62	0.11 m	0.57 m	0.65	0.11 m
EEMD-based linear fitting method	0.44 m	0.86	0 m	–	–	–	0.41 m	0.84	0.07 m	0.34 m	0.90	0.07 m
SVR-based method	0.28 m	0.94	-0.03 m	0.33 m	0.89	-0.06 m	0.32 m	0.89	0.07 m	0.25 m	0.94	0.07 m
GRU-based method	0.28 m	0.95	-0.02 m	0.34 m	0.90	-0.06 m	0.33 m	0.90	0.10 m	0.27 m	0.93	0.10 m
Proposed TCN-based method	0.26 m	0.95	0.04 m	0.32 m	0.91	0.02 m	0.32 m	0.90	0.07 m	0.24 m	0.94	0.07 m

is 0.90 when the moving average is not applied. Compared to the typical SNR-based and EEMD-based linear fitting methods, the proposed method decreases the RMSE by 0.27 m and 0.09 m with CC being furthered improved. When comparing the estimation results with the other two ML-based methods, it can be observed that while the TCN model still generates the best regression result, the difference is not significant, which indicates that the ML-based methods are superior to methods that are based on linear regression. In addition, although the proposed method performs only marginally better than the SVR-based method, the TCN-based method requires lower memory for training. This is because that the SVR-based method needs a lot of memory to store all the support vectors [89]. On the other hand, the backpropagation path of TCN can generate stable gradients and effectively mitigate the gradient of explosion [63]. Finally, it may be noted from Table 3.3 that when the moving average is applied, the estimation accuracy can be further improved. In particular, the RMSE calculated from the TCN model decreases to 0.24 m while the CC further improves to 0.94.

3.4 Chapter Summary

In this chapter, the combined features composed by SNR, EEMD and GLCM features are extracted from X-band radar image sequences to estimate H_s using a TCN-based regression model, which can derive the wave height by combining spatial and temporal features of radar

image sequences. The normalized features calculated by the SNR-, EEMD-, and GLCM-based methods are incorporated as the input feature vector for the sequence. Experiment results from nautical radar data collected from a moving vessel on the East Coast of Canada verified that the combination of all three types of features will generate the best estimation accuracy. On the other hand, the application of a moving average can effectively further improve the estimation accuracy. The proposed TCN-based method is also compared with two existing methods. It is found that compared to the typical SNR-based and EEMD-based linear fitting methods, the TCN-based model reduces the RMSEs from 0.57 m and 0.34 m to 0.24 m. Moreover, while other ML-based methods such as SVR and CGRU can also produce good results, TCN [90] is still the most accurate one. However, this proposed model should be retrained for different radars and different oceanic conditions. Thus, it is worthwhile to introduce more radar data from various radar systems and different oceanic conditions for the model training, which can make the model more robust and general. Another shortcoming of this proposed method is that the computational costs for EEMD and GLCM feature extraction are expensive. It normally takes around 65 s to produce one result. Thus, the computational load of this method needs to be reduced.

Chapter 4

Conclusion

4.1 Summary

In this thesis, sea surface wave parameters, i.e., wave direction, wave period, and H_s were retrieved and evaluated by using X-band marine radar images. When estimating the wave direction and wave period, the radar images collected under rain condition were also taken into account. Firstly, the sub-image selection scheme was proposed in order to mitigate the rain effect on the wave parameter estimation. Then, the wave direction and wave period estimation accuracy under different rainfall intensities was evaluated as well. The radar data for these two parameters were collected from an on-shore X-band marine radar at Yaquina Bay, Newport, OR, USA. A directional wave buoy located around 20 kilometers from the radar site provided simultaneous wave parameter used as ground truth. As for the sub-image selection, a random-forest-based classification method was proposed to identify the sub-image with clear wave signatures from rain-contaminated radar images. Then, those identified regions with clear wave signatures were considered as valid sub-images for the further wave direction and period estimation. In this study, an Radon transform (RT)-based method was used to estimate the wave direction from the wave signatures of selected valid sub-images. Besides this, a new random-forest-based regression method was implemented

to train the wave period estimation model using the extracted GLCM features. It is found from the experimental results that the estimation accuracies of wave direction and wave period were both improved by the application of the proposed sub-image selection scheme. Compared to the method without using sub-image selection scheme, the RMSEs of estimated wave direction using sub-image selection scheme were decreased by 6.9°, 6.0°, 4.9°, and 1.0° under rainless, light rain, moderate rain, and heavy rain conditions, respectively. On the other hand, the RMSEs of estimated wave period using sub-image selection scheme were decreased by 0.13 s, 0.20 s, 0.30 s, and 0.20 s under those four rainfall intensity levels, respectively, compared to the method without using sub-image selection scheme. Thus, the rain effect on the wave parameters can be mitigated to some extent by the sub-image selection scheme. However, under rainy conditions, the wave signatures may be still affected by rain even when the texture is clear in the sub-image identified by the selection scheme. Also, the deviations of estimated wave direction and wave period from the reference values are increased gradually with the increase of rain intensity.

As for H_s estimation, only rainless radar data were considered in this study. A TCN-based regression method was proposed to estimate H_s from the radar images. This algorithm can utilize the spatial and temporal features to analyze the radar data. In this study, the radar data were collected on a ship-borne radar around 300 km south-southeast of Halifax, Nova Scotia, Canada. Three directional wave buoys were deployed in a drifting mode to provide the simultaneous wave parameters. Firstly, three features, i.e., SNR, EEMD, and GLCM features were extracted from each radar image sequence. Then, the TCN-based regression method utilized the three features to train the H_s estimation model. According to the experimental results, it was found that the TCN-based model further improved the H_s estimation accuracy, with reductions of RMSEs by 0.33 m and 0.10 m after averaging, respectively, compared to the SNR-based and the EEMD-based linear fitting methods. It may be finally noted that for the same input features, TCN outperformed other machine learning-based algorithms including SVR and the CGRU network even though the difference was not significant.

4.2 Future Work

In the future, more image data collected from different radar systems and installation locations should be incorporated into the network to further improve the model's accuracy and robustness. Furthermore, more advanced network architectures for wave parameter estimation should be explored. Particularly, the accuracy of H_s under high wave height needs to be further improved. Besides, although the H_s estimation result is encouraging, the computational costs for the EEMD and GLCM features are expensive, i.e., it takes around one minute to produce one result. Thus, it is necessary to explore an effective way to reduce the computation cost.

In this study, the regions for wave height estimation are extracted from the upwind direction. However, the presence of swell will cause inaccuracies in the wave signatures extracted from the region in the upwind direction. Therefore, it is also necessary to consider swell when analyzing wave signatures in any future work.

Future work could also focus on the analysis of rain influence on wave height measurement from rain-contaminated X-band marine radar images. The effect of different rain intensities on H_s estimation is worth investigating, and the mitigation method of rain effect should be explored as well. Additionally, the sea surface wind gusts will also affect the surface waves, especially in the case of mesoscale convective systems [91]. Thus, the wind conditions should be included when estimating the wave parameters from radar images.

In addition, it may be meaningful to extend the research on the effects of rain in the frequency domain. Furthermore, ongoing work suggests that other sea parameters, such as current and wind can be analyzed by using more advanced ML-based methods and rain effects on these parameters can also be evaluated under different rain intensities. In conclusion, although this work is promising, more data from different radar systems and various sea states should be further investigated in the future in order to produce a more robust and general wave estimation model.

Bibliography

[1] "Yaquina bay and river marine chart," Available at http://www.gpsnauticalcharts.com/main/us18581_p1792-yaquina-bay-and-river-nautical-chart.html (2021/04/09).

[2] W. Huang, X. Liu, and E. Gill, "Ocean wind and wave measurements using X-band marine radar: A comprehensive review," *Remote Sens.*, vol. 9, no. 12, p. 1261, 2017.

[3] L.-C. Wu, D.-J. Doong, and J.-W. Lai, "Influences of nononshore winds on significant wave height estimations using coastal X-band radar images," *IEEE Trans. Geosci. Remote Sens.*, vol. 60, pp. 1–11, 2022.

[4] C. Toth and G. Jóźków, "Remote sensing platforms and sensors: A survey," *ISPRS J. Photogrammetry Remote Sens.*, vol. 115, p. 22–36, 2016.

[5] G. Engen and H. Johnsen, "SAR-ocean wave inversion using image cross spectra," *IEEE Trans. Geosci. Remote Sens.*, vol. 33, no. 4, pp. 1047–1056, 1995.

[6] B. Lipa, D. Barrick, J. Isaacson, and P. Lilleboe, "CODAR wave measurements from a north sea semisubmersible," *IEEE J. Ocean. Eng.*, vol. 15, no. 2, pp. 119–125, 1990.

[7] W. Huang, S. Wu, E. Gill, B. Wen, and J. Hou, "HF radar wave and wind measurement over the eastern china sea," *IEEE Trans. Geosci. Remote Sens.*, vol. 40, no. 9, pp. 1950–1955, 2002.

[8] I. R. Young, W. Rosenthal, and F. Ziemer, "A three-dimensional analysis of marine radar images for the determination of ocean wave directionality and surface currents," *J. Geophys. Res.-Oceans*, vol. 90, no. C1, pp. 1049–1059, 1985.

[9] R. Bürgmann, P. A. Rosen, and E. J. Fielding, "Synthetic aperture radar interferometry to measure earth's surface topography and its deformation," *Ann. Rev. Earth. Planet. Sci.*, vol. 28, no. 1, pp. 169–209, 2000.

[10] J. D. Paduan and L. K. Rosenfeld, "Remotely sensed surface currents in monterey bay from shore-based HF radar (coastal ocean dynamics application radar)," *J. Geophys. Res.*, vol. 101, no. C9, pp. 20 669–20 686, 1996.

[11] J. C. Nieto-Borge, G. R. RodrÍguez, K. Hessner, and P. I. González, "Inversion of marine radar images for surface wave analysis," *J. Atmos. Ocean. Technol.*, vol. 21, no. 8, pp. 1291–1300, 2004.

[12] C. Gommenginger, N. Ward, G. Fisher, I. Robinson, and S. Boxall, "Quantitative microwave backscatter measurements from the ocean surface using digital marine radar images," *J. Atmos. Ocean. Tech.*, vol. 17, no. 5, pp. 665–678, 2000.

[13] X. Chen and W. Huang, "Spatial-temporal convolutional gated recurrent unit network for significant wave height estimation from shipborne marine radar data," *IEEE Trans. Geosci. Remote Sens.*, vol. 60, pp. 1–11, 2022.

[14] X. Liu, W. Huang, and E. W. Gill, "Wave height estimation from shipborne X-band nautical radar images," *J. Sensors*, vol. 2016, p. 7, 2016.

[15] B. Lund, H. C. Graber, and R. Romeiser, "Wind retrieval from shipborne nautical X-band radar data," *IEEE Trans. Geosci. Remote Sens.*, vol. 50, no. 10, pp. 3800–3811, 2012.

[16] H. Dankert, J. Horstmann, and W. Rosenthal, "Ocean wind fields retrieved from radar-image sequences," *J. Geophys. Res.*, vol. 108, no. C11, 2003.

[17] B. Lund, H. C. Graber, J. Xue, and R. Romeiser, "Analysis of internal wave signatures in marine radar data," *IEEE Trans. Geosci. Remote Sens.*, vol. 51, no. 9, pp. 4840–4852, 2013.

[18] J. C. Nieto-Borge, K. Hessner, and P. Jarabo-Amores, "Signal-to-noise ratio analysis to estimate ocean wave heights from X-band marine radar image time series," *IET Radar, Sonar Navig.*, vol. 2, no. 1, pp. 35–41, 2008.

[19] J. C. Nieto-Borge and C. Guedes-Soares, "Analysis of directional wave fields using X-band navigation radar," *Coastal Eng.*, vol. 40, no. 4, pp. 375–391, 2000.

[20] R. F. Contreras and W. J. Plant, "Surface effect of rain on microwave backscatter from the ocean: Measurements and modeling," *J. Geophys. Res. Oceans*, vol. 111, no. C8, pp. 1–18, 2006.

[21] X. Chen and W. Huang, "Identification of rain and low-backscatter regions in X-band marine radar images: an unsupervised approach," *IEEE Trans. Geosci. Remote Sens.*, vol. 58, no. 6, pp. 4225–4236, 2020.

[22] Y. Wang and W. Huang, "An algorithm for wind direction retrieval from X-band marine radar images," *IEEE Geosci. Remote. Sens. Lett.*, vol. 13, no. 2, pp. 252–256, 2016.

[23] J. Wright, "Backscattering from capillary waves with application to sea clutter," *IEEE Trans. Antennas Propag.*, vol. 14, no. 6, pp. 749–754, 1966.

[24] M. Mattie and D. L. Harris, "A system for using radar to record wave direction," *Tech. Rep., U.S. Army Corps of Eng. , Coast. Eng. Res. Ctr., Fort Belvoir*, vol. 79-1, p. 50, 1979.

[25] F. Ziemer, W. Rosenthal, and H. Carlson, "Measurements of directional wave spectra by ship radar," *IAPSO Symp., General Assembly, Int. Assoc. Phys. Sci. Oceans, Hamburg*, 1983.

[26] V. Atanassov, W. Rosenthal, and F. Ziemer, "Removal of ambiguity of twodimensional power spectra obtained by processing ship radar images of ocean waves," *J. Geophys. Res.*, vol. 90, no. C1, pp. 1061–1067, 1985.

[27] K. Reichert, K. Hessner, J. C. Nieto-Borge, and J. Dittmer, in *Proc. 9th ISOPE*, Brest, France.

[28] P. Izquierdo, C. Guedes-Soares, J. Nieto-Borge, and G. Rodríguez, "A comparison of sea-state parameters from nautical radar images and buoy data," *Ocean Eng.*, vol. 31, no. 17-18, pp. 2209–2225, 2004.

[29] L. Cui, Y. He, H. Shen, and H. Lu, "Measurements of ocean wave and current field using dual polarized X-band radar," *Chin. J. Oceanol. Limnol.*, vol. 28, p. 1021–1028, 2010.

[30] W. Alpers, D. Ross, and C. Rufenach, "On the detectability of ocean surface waves by real and synthetic aperture radar," *J. Geophys. Res.*, vol. 86, no. C7, pp. 6481–6498, 1981.

[31] W. Plant and L. Zurk, "Dominant wave directions and significant wave heights from synthetic aperture radar imagery of the ocean," *J. Geophys. Res.*, vol. 102, pp. 3473–3482, 1997.

[32] J. Nieto-Borge, K. Hessner, and K. Reichert, "Estimation of the significant wave height with X-band nautical radars," in *Proc. 18th Int. Conf. Offshore Mechanics and Arctic Engineering (OMAE), Newfoundland, Canada*, 1999.

[33] C. M. Senet, J. Seemann, and F. Ziemer, "The near-surface current velocity determined from image sequences of the sea surface," *IEEE Trans. Geosci. Remote Sens.*, vol. 39, no. 3, pp. 492–505, 2001.

[34] C. Stevens, E. Poulter, M. Smith, and J. McGregor, "Nonlinear features in wave-resolving microwave radar observations of ocean waves," *IEEE J. Ocean. Eng.*, vol. 24, no. 4, pp. 470–480, 1999.

[35] Y. Wei, Z. Lu, G. Pian, and H. Liu, "Wave height estimation from shadowing based on the acquired X-band marine radar images in coastal area," *Remote Sens.*, vol. 9, no. 8, p. 859, 2017.

[36] X. Liu, W. Huang, and E. W. Gill, "Estimation of significant wave height from X-band marine radar images based on ensemble empirical mode decomposition," *IEEE Geosci. Remote. Sens. Lett.*, vol. 14, no. 10, pp. 1740–1744, 2017.

[37] W. Huang, E. Gill, and J. An, "Iterative least-squares-based wave measurement using X-band nautical radar," *IET Radar, Sonar Navig.*, vol. 8, no. 8, pp. 853–863, 2014.

[38] A. Al-Habashneh, C. Moloney, E. Gill, and W. Huang, "An adaptive method of wave spectrum estimation using X-band nautical radar," *Remote Sens.*, vol. 7, no. 12, p. 16537–16554, 2015.

[39] L. Wang, X. Wu, X. Yue, K. Ma, and Y. Tian, "A novel algorithm in estimating signal-to-noise ratio for ocean wave height inversion from X-band radar images," *IEEE Geosci. Remote. Sens.*, vol. 13, no. 3, pp. 344–348, 2016.

[40] J. An, W. Huang, and E. W. Gill, "A self-adaptive wavelet-based algorithm for wave measurement using nautical radar," *IEEE Trans. Geosci. Remote Sens.*, vol. 53, no. 1, p. 567–577, 2015.

[41] K. Ma, X. Wu, X. Yue, L. Wang, and J. Liu, "Array beamforming algorithm for estimating waves and currents from marine X-band radar image sequences," *IEEE Trans. Geosci. Remote Sens.*, vol. 55, no. 3, p. 1262–1272, 2017.

[42] B. Van Veen and K. Buckley, "Beamforming: a versatile approach to spatial filtering," *IEEE ASSP Magazine*, vol. 5, no. 2, pp. 4–24, 1988.

[43] J. Buckley and J. Aler, "Estimation of ocean wave height from grazing incidence microwave backscatter," in *Proc. IEEE Int. Geosci. Remote Sens. Symp.*, vol. 2, Singapore, 1997, pp. 1015–1017.

[44] ——, "Enhancements in the determination of ocean surface wave height from grazing incidence microwave backscatter," in *Proc. IEEE Int. Geosci. Remote Sens. Symp.*, vol. 5, Seattle, WA, USA, 1998, pp. 2487–2489.

[45] R. Gangeskar, "Wave height derived by texture analysis of X-band radar sea surface images," in *Proc. IEEE Int. Geosci. Remote Sens. Symp.*, vol. 7, Honolulu, HI, USA, 2000, pp. 2952–2959.

[46] ——, "An adaptive method for estimation of wave height based on statistics of sea surface images," in *Proc. IEEE Int. Geosci. Remote Sens. Symp.*, vol. 1, Honolulu, HI, USA, 2000, pp. 255–259.

[47] H. Dankert, J. Horstmann, and W. Rosenthal, "Wind- and wave-field measurements using marine X-band radar-image sequences," *IEEE J. Ocean. Eng.*, vol. 30, no. 3, pp. 534–542, 2005.

[48] X. Liu, W. Huang, and E. W. Gill, "An algorithm for estimation of wave parameters from X-band marine radar images," in *Proc. 2018 IEEE Radar Conf. (RadarConf18)*, 2018, pp. 0095–0099.

[49] R. Gangeskar, "An algorithm for estimation of wave height from shadowing in X-band radar sea surface images," *IEEE Trans. Geosci. Remote Sens.*, vol. 52, no. 6, pp. 3373–3381, 2014.

[50] Z. Chen, Y. He, and B. Zhang, "An automatic algorithm to retrieve wave height from X-band marine radar image sequence," *IEEE Trans. Geosci. Remote Sens.*, vol. 55, no. 9, pp. 5084–5092, 2017.

[51] S. Salcedo-Sanz, J. Nieto-Borge, L. Carro-Calvo, L. Cuadra, K. Hessner, and E. Alexandre, "Significant wave height estimation using SVR algorithms and shadowing information from simulated and real measured X-band radar images of the sea surface," *Ocean Eng.*, vol. 101, no. 1, p. 244–253, 2015.

[52] L. Cornejo-Bueno, J. Nieto-Borge, E. Alexandre, K. Hessner, and S. Salcedo-Sanz, "Accurate estimation of significant wave height with support vector regression algorithms and marine radar images," *Coastal Eng.*, vol. 114, pp. 233–243, 2016.

[53] R. Vicen-Bueno, C. Lido-Muela, and J. Nieto-Borge, "Estimate of significant wave height from non-coherent marine radar images by multilayer perceptrons," *EURASIP J. Adv. Signal Process.*, vol. 2012, no. 84, 2012.

[54] J. Park, K. Ahn, C. Oh, and Y. S. Chang, "Estimation of significant wave heights from X-band radar using artificial neural network," *J. Korean Soc. Coast. Ocean. Eng.*, vol. 32, no. 6, p. 561–568, 2020.

[55] W. Duan, K. Yang, L. Huang, and X. Ma, "Numerical investigations on wave remote sensing from synthetic X-band radar sea clutter images by using deep convolutional neural networks," *Remote Sens.*, vol. 12, no. 7, p. 1117, 2020.

[56] J. Shen, Y. Li, Y. Dai, and S. Wang, "Identification and suppression of rain interference on X-band radar images," *Opt. Precis. Eng.*, vol. 20, no. 8, pp. 1846–1853, 2012.

[57] X. Chen, W. Huang, C. Zhao, and Y. Tian, "Rain detection from X-band marine radar images: A support vector machine-based approach," *IEEE Trans. Geosci. Remote Sens.*, vol. 58, no. 3, pp. 2115–2123, 2020.

[58] Y. Liu, W. Huang, and E. W. Gill, "Analysis of the effects of rain on surface wind retrieval from X-band marine radar images," in *Proc. 2014 Oceans - St. John's*, 2014, pp. 1–4.

[59] W. Huang, X. Liu, and E. W. Gill, "An empirical mode decomposition method for sea surface wind measurements from X-band nautical radar data," *IEEE Trans. Geosci. Remote Sens.*, vol. 55, no. 11, pp. 6218–6227, 2017.

[60] X. Chen, W. Huang, and G. Yao, "Wind speed estimation from X-band marine radar images using support vector regression method," *IEEE Trans. Geosci. Remote Sens. Letters*, vol. 15, no. 9, pp. 1312–1316, 2018.

[61] Z. Chen, Y. He, B. Zhang, and Y. Ma, "A method to correct the influence of rain on X-band marine radar image," *IEEE Access*, vol. 5, pp. 25 576–25 583, 2017.

[62] W. Huang, Y. Liu, and E. Gill, "Texture-analysis-incorporated wind parameters extraction from rain-contaminated X-band nautical radar images," *Remote Sens.*, vol. 9, no. 2, p. 166, 2017.

[63] S. Bai, J. Z. Kolter, and V. Koltun, "An empirical evaluation of generic convolutional and recurrent networks for sequence modeling," *arXiv: 1803.01271*, 2018.

[64] M. A. Mason, "The transformation of waves in shallow water," *Coast. Eng. Proc.*, vol. 1, no. 1, p. 3, Jan. 1950. [Online]. Available: https://journals.tdl.org/icce/index.php/icce/article/view/906

[65] H. H. Shih, "Triaxys directional wave buoy for nearshore wave measurements: test and evaluation plan," *NOAA technical report NOS CO-OPS 38*, 2003.

[66] R. M. Haralick, K. Shanmugam, and I. Dinstein, "Textural features for image classification," *IEEE Trans. Syst., Man, and Cyber.*, vol. SMC-3, no. 6, pp. 610–621, 1973.

[67] R. Keys, "Cubic convolution interpolation for digital image processing," *IEEE Trans. Acoust. Speech Signal Process.*, vol. 29, no. 6, pp. 1153–1160, 1981.

[68] L. Breiman, "Random forests," *Mach. Learn.*, vol. 45, no. 1, pp. 5–32, 2001.

[69] B. Efron and R. Tibshirani, "Improvements on cross-validation: The 632+ bootstrap method," *J. Am. Stat. Assoc.*, vol. 92, no. 438, pp. 548–560, 1997.

[70] L. Breiman, J. H. Friedman, R. A. Olshen, and C. J. Stone, *Classification and Regression Trees*. California: Wadsworth Int., 1984.

[71] J. Canny, "A computational approach to edge detection," *IEEE Trans. Pattern Anal. Mach. Intell.*, vol. PAMI-8, no. 6, pp. 679–698, 1986.

[72] J. Radon, "Über die bestimmung von funktionen durch ihre integralwerte längs gewisser mannigfaltigkeiten," *Math. Phys. Klasse*, vol. 69, p. 262–277, 1917.

[73] Z. Chen, Y. He, B. Zhang, Z. Qiu, and B. Yin, "A new algorithm to retrieve wave parameters from marine X-band radar image sequences," *IEEE Trans. Geosci. Remote Sens.*, vol. 52, no. 7, pp. 4083–4091, 2014.

[74] J. Xie, J. Zhang, X. Xie, Z. Bi, and Z. Li, "Ensemble of bagged regression trees for concrete dam deformation predicting," *IOP Conf. Ser.: Earth Environ. Sci.*, vol. 376, 2019.

[75] Environment and Climate Change Canada, *Manual of surface weather observations standards (MANOBS), 8th Edition*, Available at http://publications.gc.ca/collections/collection_2019/eccc/En56-238-2-2018-eng.pdf, 2019.

[76] K. Dobbin and R. Simon, "Optimally splitting cases for training and testing high dimensional classifiers," *BMC Med. Genomics*, vol. 4, no. 31, 2011.

[77] D. Stredulinsky and E. Thornhill, "Ship motion and wave radar data fusion for shipboard wave measurement," *J. Sh. Res.*, vol. 55, no. 2, p. 73–85, 2011.

[78] C. Shen, W. Huang, E. W. Gill, R. Carrasco, and J. Horstmann, "An algorithm for surface current retrieval from X-band marine radar images," *Remote Sens.*, vol. 7, no. 6, pp. 7753–7767, 2015.

[79] J. Nieto-Borge, K. Reichert, and K. Hessner, "Detection of spatio-temporal wave grouping properties by using temporal sequences of X-band radar images of the sea surface," *Ocean Modelling*, vol. 61, pp. 21–37, 2013.

[80] N. E. Huang, Z. Wu, S. R. Long, K. C. Arnold, X. Chen, and K. Blank, "On instantaneous frequency," *Adv. Adapt. Data Anal.*, vol. 1, no. 2, p. 177–229, 2009.

[81] Z. Yang, W. Huang, and X. Chen, "Evaluation and mitigation of rain effect on wave direction and period estimation from X-band marine radar images," *IEEE J. Sel. Top. Appl. Earth Obs. Remote Sens.*, vol. 14, pp. 5207–5219, 2021.

[82] F. Yu and V. Koltun, "Multi-scale context aggregation by dilated convolutions," *In ICLR*, 2016.

[83] V. Nair and G. Hinton, "Rectified linear units improve restricted boltzmann machines," in *Proc. Intl. Conf. Mach. Learn.*, 2010.

[84] N. Srivastava, G. Hinton, A. Krizhevsky, I. Sutskever, and R. Salakhutdinov, "Dropout: A simple way to prevent neural networks from overfitting," *J. Mach. Learn. Res.*, vol. 15, no. 1, p. 1929–1958, 2014.

[85] K. He, X. Zhang, S. Ren, and J. Sun, "Deep residual learning for image recognition," *in Proc. IEEE Comput. Soc. Conf. Comput. Vis. Pattern Recognit. (CVPR)*, 2016.

[86] D. Kingma and J. Ba, "Adam: A method for stochastic optimization," *ArXiv:1412.6980*, 2015.

[87] A. Smola and B. Schölkopf, "A tutorial on support vector regression," *Stat. Comput.*, vol. 14, p. 199–222, 2004.

[88] J. Chung, C. Gulcehre, K. Cho, and Y. Bengio, "Empirical evaluation of gated recurrent neural networks on sequence modeling," *arXiv:1412.3555*, 2014. [Online]. Available: https://arxiv.org/abs/1412.3555

[89] S. Durgam, A. Bhosale, V. Bhosale, R. Deshpande, and P. Sutar, "Support vector regression method for predicting temperatures of heat sources cooled by forced convection in a horizontal channel," *Therm. Sci. Eng. Prog.*, vol. 20, p. 100725, 2020. [Online]. Available: https://www.sciencedirect.com/science/article/pii/S2451904920302456

[90] W. Huang, Z. Yang, and X. Chen, "Wave height estimation from X-band nautical radar images using temporal convolutional network," *IEEE J. Sel. Topics Appl. Earth Observ. Remote Sens.*, vol. 14, pp. 11 395–11 405, 2021.

[91] I. L. Jirak, W. R. Cotton, and R. L. McAnelly, "Satellite and radar survey of mesoscale convective system development," *Mon. Weather Rev.*, vol. 131, no. 10, pp. 2428–2449, 2003.